Thermodynamics of strain-induced crystallization in filled natural rubber under uni- and biaxial loadings, Part II: Physically-based constitutive theory

V. N. Khiem, Jean-Benoit Le Cam, Sylvain Charles, M. Itskov

Thermodynamics of strain-induced crystallization in filled natural rubber under uni- and biaxial loadings. Part II: Physically-based constitutive theory.

V. N. Khiêm[a,*], J. B. Le Cam[b], S. Charlès[b], M. Itskov[a]

[a] *Department of Continuum Mechanics, RWTH Aachen University, Eilfschornsteinstr. 18 , 52062 Aachen, Germany*

[b] *Institut de Physique UMR 6251 CNRS/Université de Rennes 1, Rennes, France*

Abstract

To understand thoroughly the strain-induced crystallization in natural rubbers, conventional mechanical measurements are inadequate because they only provide a macroscopic relation between stress and strain. In this second part, a physically-based constitutive model for filled natural rubbers is coupled with the infrared thermography based quantitative surface calorimetry (Part I) to shed new light on multiaxiality of strain-induced crystallization. In contrast to previous works, the kinetics of phase transition outside thermodynamic equilibrium is discussed. By introducing only two additional parameters (compared to the equilibrium crystallization theory), underlying mechanisms of nonequilibrium strain-induced crystallization can be well interpreted. To capture multiaxiality of strain-induced crystallinity, the analytical network-averaging is utilized for the calculation of kinematic internal variables. Model predictions are then compared with comprehensive testing data (Part I) and demonstrate good agreement with these experiments.

Keywords: Filled natural rubber, Analytical network-averaging, Dynamics of strain-induced crystallization, Nonequilibrium, Calorimetric effect, Multiaxial tension

*Corresponding author

Email address: khiem.vu@rwth-aachen.de (V. N. Khiêm)

1. Introduction

The crystallization of natural rubber under deformation (so-called strain induced crystallization, Katz (1925)) is believed to be crucial for its resistance to crack growth. Most of studies on strain-induced crystallization for the last two decades were conducted under the quasi-static conditions (see a thorough review in Khiêm and Itskov (2018b)). Although very important, there have been relatively few studies on strain-induced crystallization under dynamic loading. It has been reported that, natural rubber demonstrates lower crack resistance under dynamic loading compared to quasi-static one (Huneau, 2011). The crystallinity is lower whereas the stress is higher as the deformation rate increases (Rault et al., 2006a; Amnuaypornsri et al., 2012; Candau et al., 2015; Brüning et al., 2012). When natural rubber is subjected to a constant strain, the stress gradually decreases and the crystallinity increases (Rault et al., 2006a; Tosaka et al., 2006; Brüning et al., 2015). Due to the little experimental research on dynamic loading, thermomechanics and kinetics of the strain-induced crystallization have not been fully understood despite the recent effort on theoretical treatments (Laghmach et al., 2015; Plagge and Klüppel, 2018; Plagge and Hentschke, 2021; Khiêm and Itskov, 2018b; Gros et al., 2019a).

The constitutive modeling of strain-induced crystallization in natural rubbers were solely considered in either equilibrium or nonequilibrium situation. The rate-independent elastoplasticity has been extensively used in constitutive modeling of strain-induced crystallization (Mistry and Govindjee, 2014; Guilié et al., 2015; Rastak and Linder, 2018; Guo et al., 2018; Nateghi et al., 2018; Aygün and Klinge, 2020; Arunachala et al., 2021). Since the crystallinity there was considered as an elastoplastic internal variable, these models can only describe the decrease of stress after the onset of strain-induced crystallization (compared to noncrystallizing rubber) but cannot predict the stress upturn afterwards. Dargazany et al. (2014a,b); Plagge and Klüppel (2018); Plagge and Hentschke (2021); Gros et al. (2019b) modeled strain-induced crystallization by rate-independent damage evolutions, which are subjected to the same issues as elastoplasticity models. Furthermore, since damage-elastoplastic models are rate-independent, they cannot capture time-dependent strain-induced crystallization

(Brüning et al., 2012). Last but not least, all these models result in strictly positive intrinsic dissipation in quasi-static loading, which contradicts experimental observation (Samaca Martinez et al., 2013b). Other researchers (Kroon, 2010; Guo and Zaïri, 2020; Loos et al., 2020) made use of rate-dependent flow-rule to describe strain-induced crystallization. All mentioned constitutive models are isothermal, which also disagrees with experimental observations (Candau et al., 2015; Samaca Martinez et al., 2013a). Recently, Behnke et al. (2018) developed a phenomenological model for thermo-mechanical coupling in nonequilibrium crystallization, however their model cannot describe the decrease of stress at the onset of strain-induced crystallization. Khiêm and Itskov (2018b) proposed a quasi-static constitutive theory for strain-induced crystallization in natural rubbers which can reproduce both mechanical and calorimetric response of natural rubbers. Moreover, their theory proves that the intrinsic dissipation in natural rubber under quasi-static loading is zero (Samaca Martinez et al., 2013b), and the quasi-static hysteresis is due to the appearance of a second type of crystallites under unloading. Nevertheless, this model does not cover nonequilibrium aspects of strain-induced crystallization.

In this contribution, we investigate the dynamics of strain-induced crystallization from the theoretical point of view. We aim to answer three fundamental questions: What are similarities and differences between equilibrium and nonequilibrium strain-induced crystallization? What are sources of hysteresis in dynamic loading of natural rubbers? Can natural rubbers crystallize under biaxial loading? To this end, the previous theory of equilibrium strain-induced crystallization (Khiêm and Itskov, 2018b) will be considerably extended outside of the thermodynamic equilibrium. Furthermore, a fully non-adiabatic thermodynamic process will be considered here. The advanced experimental result of Part I (Khiêm et al., 2021) will be utilized for the validation of the theory. Sections 2 - 5 of the paper discuss newly developed concepts in multiaxiality, strain-induced crystallization and filler-polymer interaction in filled natural rubbers. Sophisticated analysis (Section 7) of the theoretical model (Section 6) reveals a full picture of dynamics of crystallization induced by multiaxial tension. Additionally, four appendices summarize important results of the previous theories (Khiêm and Itskov, 2017) and (Khiêm and Itskov, 2018b) are included for reader

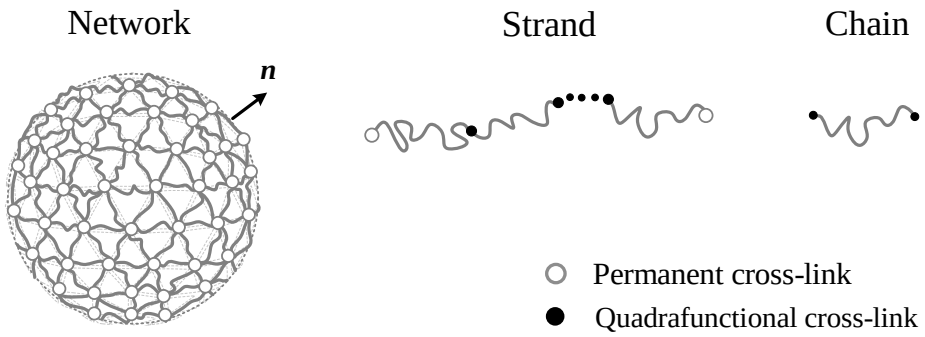

Figure 1: Polymer network, strand and chain (Khiêm et al., 2019).

convenience.

2. Kinematics

2.1. Terminology

In this paper, we consider a polymer network as a composition of many linear polymer strands (so-called subnetworks) dispersed in different directions $\boldsymbol{n}$ in space (Figure 1, Khiêm and Itskov (2016)). A strand is defined by a subnetwork path between two permanent cross-links whose functionalities could be three or more. Each polymer strand contains a series of chains. A chain is defined as a part of strand between two successive quadrafunctional cross-links (e.g. trapped entanglements).

2.2. Kinematic measure

According to the analytical network-averaging concept (Khiêm and Itskov, 2017; Khiêm et al., 2019), the average stretch applied on the polymer strand in a direction i in the filled rubber network can be given by

$$\bar{\Lambda}_{\mathrm{i}} = \left(\int_S \rho_{\mathrm{i}}\left(\boldsymbol{n}\right) \overset{\boldsymbol{n}}{\Lambda^2}\, dS \right)^{\frac{1}{2}} = \left(\left(1 - w_0\right) \frac{I_1}{3} + w_0 \Lambda_{\mathrm{i}}^2 \right)^{\frac{1}{2}}. \qquad \mathrm{i} = 1, 2, .., m, \tag{1}$$

where m is the number of equidistant points on the microsphere (see Appendix A). Furthermore, $\rho_{\mathrm{i}}\left(\boldsymbol{n}\right)$ is the directional probability distribution function of polymer strands (its

specific form is given in Appendix A), $\boldsymbol{n}$ is an arbitrary direction in the microsphere representing the directional random variable. I_1 represents the first principal invariant of the right Cauchy-Green tensor $\mathbf{C} = \mathbf{F}^{\mathrm{T}}\mathbf{F}$, where $\mathbf{F}$ is the deformation gradient, and $\Lambda_{\mathrm{i}}^2 = \mathbf{C} : \boldsymbol{E}_{\mathrm{i}} \otimes \boldsymbol{E}_{\mathrm{i}}$ denotes the square of the principal stretch in a direction specified by a unit vector $\boldsymbol{E}_{\mathrm{i}}$. Furthermore, w_0 is the effective volume fraction of filler (Khiêm and Itskov, 2017). The average stretch (1) captures the interpenentration of polymer strands in different directions (Khiêm et al., 2019), which is crucial for describing multiaxiality of polymeric materials at finite strain. In the current paper, this kinematic measure will be applied for the case of strain-induced crystallization.

3. Strain-induced crystallization

In this section, a novel multiple-step kinetics of strain-induced crystallization is discussed. This involves the nucleation of the primary crystallites, independent nucleation and growth of secondary crystallites, as well as dependent growth of tertiary crystallites (Figure 2).

To describe the dynamics of strain-induced crystallization, static and free strands in the natural rubber network are considered. The crystallization in static strands (with a fraction of $\Phi = 2/3$) is time-independent, while the free strands (with a fraction $(1 - \Phi)$) can undergo unequilibrium crystallization. The free strand are long chains with the number of chain segments significantly higher than the static chains. Since these two strand types are independent, the total crystallinity is a sum of equilibrium crystallinity $\Phi\zeta^{eq}$ and nonequilibrium crystallinity ζ

$$\zeta^{total} = \Phi\zeta^{eq} + \zeta. \tag{2}$$

Before discussing the unequilibrium crystallization, let us recall the previous derivation of crystallinity at equilibrium (Khiêm and Itskov, 2018b).

3.1. Equilibrium crystallinity

According to the previous equilibrium theory of crystallization (Khiêm and Itskov, 2018b), the crystallization in natural rubbers contains two steps: formation of a solid cluster of poly-

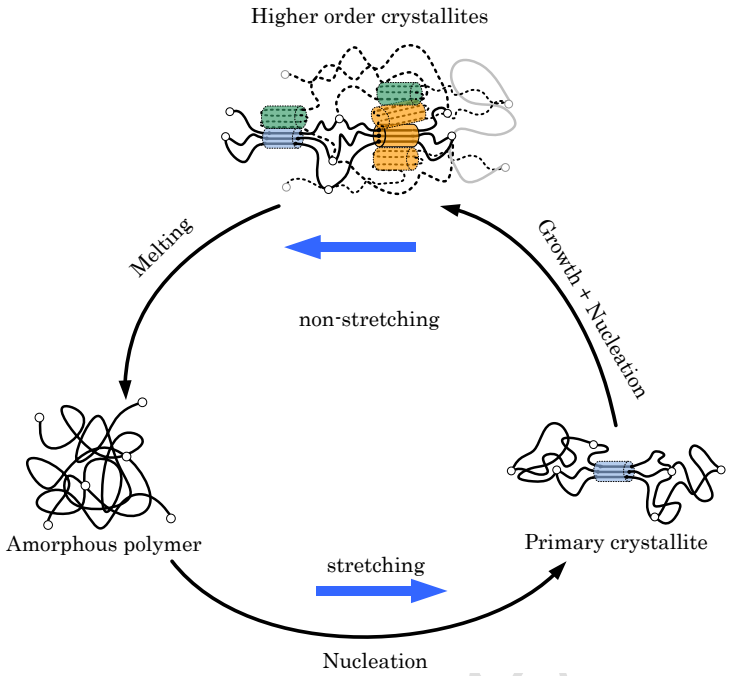

Figure 2: Crystallization kinetics (filled circles represent either physical or chemical cross-links): Primary crystallites (blue) nucleate in stretched polymer strands. Higher order crystallites (secondary-orange or tertiary-green) develop during non-stretching states (i.e. unloading or stress relaxation). The secondary crystallites occur during unloading, they can nucleate, grow and melt independently from the primary crystallites. The tertiary ones can only grow on existing crystallites (either primary or secondary) during stress relaxation. They will disappear when their nuclei melt.

mer segments (nucleus) in the amorphous network and growth of such cluster (Appendix B). The former is referred to as crystallization nucleation (Fig.3) which can occur in both loading and unloading, while the latter is referred to as crystallization growth solely taking place in unloading.

The equilibrium crystallinity due to nucleation can be given by (see details in Appendix B)

$$\zeta_{\mathrm{I}}^{eq} = \sum_{i=1}^{m} \zeta_{\mathrm{I}i}^{eq} = \sum_{i=1}^{m} B_1 \exp\left(-\frac{8\pi\gamma_t\gamma_s^2}{k_{\mathrm{B}}T_0\Delta\Psi_{\mathrm{i}}^2\left(\bar{\Lambda}_{\mathrm{i}}\right)}\right), \tag{3}$$

where γ_t, γ_s are the surface tension at the top and the side surfaces of the crystallite, respectively. T_0 is the reference (absolute) temperature and k_{B} is the Boltzmann constant.

The analytical network-averaging (A.3) requires a calculation of the fraction of oriented

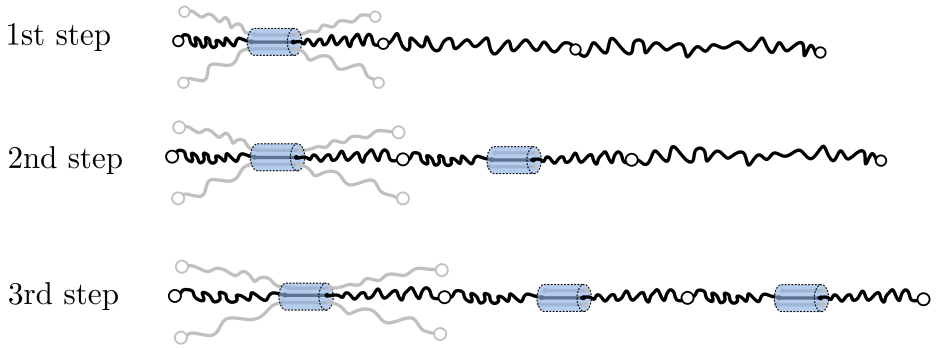

Figure 3: Crystallization nucleation: In the first step, the nucleus size reach the critical dimension, so that a crystallite is formed in the strand. Next, the deformation increases, the nucleation occurs in a neighboring chain in the strand (action at distance), therefore there are 2 crystallites in the strand. Further stretching lead to more and more crystallites in the network strand. Until all chains in the strand become semi-crystalline, the saturation of crystallization nucleation takes place.

strands. In the case of strain-induced crystallization, the fraction of oriented strands in each direction is proportional to the directional crystallinity and is expressed as

$$w_i = w_0 + w_L \exp\left(-\frac{8\pi\gamma_t\gamma_s^2}{k_{\mathrm{B}}T_0\Delta\Psi_{\mathrm{i}}^2\left(\bar{\Lambda}_{\mathrm{i}}\right)}\right), \tag{4}$$

where $w_L = 30\%$ is the maximum fraction of chain alignment (Toki et al., 2002; Murakami et al., 2002; Toki et al., 2003).

The change in the free energy $\Delta\Psi_{\mathrm{i}}$ of the pure polymer strand (i.e. without crystallites) can be obtained as (Khiêm and Itskov, 2016)

$$\Delta\Psi_{\mathrm{i}}\left(\bar{\Lambda}_{\mathrm{i}}\right) = w_{\mathrm{L}}\frac{N_{\mathrm{c0}}}{m}k_{\mathrm{B}}T_0\kappa n \ln\left(\frac{\sin\frac{\pi}{\sqrt{n}}\cdot\bar{\Lambda}_{\mathrm{i}}}{\sin\left(\frac{\pi}{\sqrt{n}}\Lambda_{\mathrm{i}}\right)}\right), \qquad \mathrm{i} = 1, 2, ..m, \tag{5}$$

where N_{c0} is the total number of chains per unit reference volume of the rubber network, n is the average number of chain segments in the semi-crystalline network, and $\kappa = \dfrac{9}{\pi^2}$ (Khiêm and Itskov, 2016).

Furthermore, the equilibrium crystallinity due to crystallization growth is expressed as

(see details in Appendix B)

$$\zeta_{\mathrm{II}}^{eq} = \sum_{i=1}^{m} B_2 \exp\left(-\frac{8\pi\bar{\gamma}_t\bar{\gamma}_s^2}{k_{\mathrm{B}}T_0\Delta\Psi_{\mathrm{i}}^2}\right)\left[\exp\left(-\frac{8\pi\bar{\gamma}_t\bar{\gamma}_s^2}{k_{\mathrm{B}}T_0\Delta\Psi_{\mathrm{i}}^2\left(\bar{\Lambda}_{\mathrm{i}}^{c\max}\right)}\right) - \exp\left(-\frac{8\pi\bar{\gamma}_t\bar{\gamma}_s^2}{k_{\mathrm{B}}T_0\Delta\Psi_{\mathrm{i}}^2\left(\bar{\Lambda}_{\mathrm{i}}\right)}\right)\right], \tag{6}$$

where new surface tensions $\bar{\gamma}_t$ and $\bar{\gamma}_s$ are used because the morphology of the secondary crystallite is different from that of the primary crystallite. To be consistent with Khiêm and Itskov (2018b), we set $\bar{\gamma}_t\bar{\gamma}_s^2 = \dfrac{\gamma_t\gamma_s^2}{\chi^2}$. Therein, the relative ratio of surface tension $\chi > 1$ indicates that it is easier to attach a polymer segment to the secondary crystallite than to the primary one. Thus, the melting point is lower than the onset of strain-induced crystallization ($\Lambda_m < \Lambda_c$) due to the introduction of a new crystal morphology. The former term in the product (6) represents the crystallinity of crystal nuclei, while the latter is the fraction of grown crystallites.

The maximal cyclic stretch $\bar{\Lambda}_{\mathrm{i}}^{c\max}$ is an internal variable, which can be defined as

$$\bar{\Lambda}_{\mathrm{i}}^{c\max} = \max_{\tau\in\left[t_{\mathrm{i}}^{c},t\right]} \bar{\Lambda}_{\mathrm{i}}(\tau), \qquad \mathrm{i} = 1, 2, .., m, \tag{7}$$

where the ending time of the closest directional loading cycle t_{i}^{c} is defined by the local minimum of $\bar{\Lambda}_{\mathrm{i}}^{\mathrm{e}}$ within the time interval $\tau \in (-\infty, t]$. As shown in Khiêm and Itskov (2018b), the internal variable $\bar{\Lambda}_{\mathrm{i}}^{c\max}$ is essential for the description of equilibrium crystallization. It should be noted that during loading $\zeta_{\mathrm{II}}^{eq} = 0$, so that secondary crystallites only form in the direction with a negative stretch rate.

In view of (3) and (6) the total crystallinity at equilibrium is calculated as

$$\zeta^{eq} = \zeta_{\mathrm{I}}^{eq} + \zeta_{\mathrm{II}}^{eq}. \tag{8}$$

3.2. Nonequilibrium crystallinity

Outside of thermodynamic equilibrium, the crystallinity can develop (from previously existed nuclei) and melt spontaneously. Let $\zeta(t)$ be the total crystallinity in a representative

free strand at time t. In view of (2), the maximal crystallinity of nuclei in the material is $(1-\Phi)\zeta^{eq}(t)$. Without loss of generality, we assume that the melting rate and nucleation rate per crystallinity are the same and can be given by τ_n^{-1}. Thus, the change in nonequilibrium crystallinity within a time increment Δt is equal to the difference between nucleation and melting crystallinities, so that

$$\frac{\zeta\left(t+\Delta t\right)-\zeta\left(t\right)}{\Delta t}=(1-\Phi)\frac{\zeta^{eq}}{\tau_n}-\frac{\zeta}{\tau_n}, \tag{9}$$

where τ_n is the characteristic time of nonequilibrium crystallization nucleation and melting.

Taking the limit $\Delta t \to 0$ and assuming ζ is differentiable yield the following evolution law for the nonequilibrium crystallinity

$$\begin{cases} \dot{\zeta}+\dfrac{\zeta}{\tau_n}=\dfrac{(1-\Phi)\zeta^{eq}}{\tau_n}, \\ \zeta\left(0\right)=0. \end{cases} \tag{10}$$

The first order differential equation (10) enables interpretation of the underlying mechanism of crystallization under multiple situations. First, due to the additive nature of (8), $\zeta=\zeta_{\mathrm{I}}+\zeta_{\mathrm{II}}$, where ζ_{I}, ζ_{II} are the nonequilibrium crystallinity of primary and secondary crystallites, respectively. Thus, the same mechanisms as described in Section 3.1 take place in dynamic loading: nucleation of primary crystallites during loading, growth and melting of the two types of crystallites (primary and secondary) during unloading. Second, during pure dynamic loading (i.e. without relaxation), by substituting $\zeta=\zeta_{\mathrm{I}}$ into (10), the solution of (10) reads

$$\zeta_{\mathrm{I}}=\int_0^t \exp\left(\frac{s-t}{\tau_n}\right)\frac{(1-\Phi)\zeta_{\mathrm{I}}^{eq}\left(s\right)}{\tau_n}ds. \tag{11}$$

In view of the comparison theorem, (11) indicates that the total crystallinity (2) during dynamic stretching is lower than ζ_{I}^{eq}, which is inline with experimental observation (Brüning et al., 2012).

Furthermore, during stress relaxation where $(1-\Phi)\zeta^{eq} = const$, the solution of (10) is given by

$$\zeta = (1-\Phi)\zeta^{eq}\left(1-\exp\left(-\frac{t}{\tau_n}\right)\right). \tag{12}$$

Dividing (12) by the the crystallinity at the starting point of relaxation ζ_R yields the total grown crystallinity during relaxation as

$$\zeta_{\text{III}} = (1-\Phi)\zeta^{eq}\left(\exp\left(-\frac{t_R}{\tau_n}\right)-\exp\left(-\frac{t+t_R}{\tau_n}\right)\right), \tag{13}$$

where the scalar $t_R = \tau_n \ln \zeta_R$. (13) describes the growth of tertiary crystallites from either primary crystallites (during loading) or from both primary and secondary ones (during unloading), see Fig.2.

Remark 1. *In thermodynamic equilibrium, the differential equation* (10) *results in* $\zeta = (1-\Phi)\zeta^{eq}$. *In view of* (2)*, the current theory reproduces the previous equilibrium crystallization* ζ^{eq} *(Khiêm and Itskov, 2018b). In this case,* (10) *also resembles the classical nucleation kinetics (Wakeshima, 1954).*

4. Semi-crystalline network

As there are static chains and free chains corresponding to equilibrium and nonequilibrium crystallization in natural rubbers, we shall derive the free energy densities for the two cases.

4.1. Equilibrium semi-crystalline chains (static chains)

According to the analytical network averaging concept (Khiêm and Itskov, 2016, 2017, 2018a,b; Khiêm et al., 2019), one can replace all chains in the semi-crystalline network by a representative chain subject to a microscopic stretch and a microscopic tube contraction. For the sake of simplicity, we neglect the energetic contribution of crystallites during loading and consider only their entropic effect (Khiêm and Itskov, 2018b). The microscopic stretch

can be given by (Khiêm and Itskov, 2018b)

$$\bar{\lambda} = \bar{\Lambda}^q, \tag{14}$$

where q is the stretch amplification exponent approximated in the case of strain-induced crystallization by (Khiêm and Itskov, 2018b)

$$q = q_0(1 + \zeta_b), \tag{15}$$

where $\zeta_b = \Phi\zeta_{\mathrm{I}}^{eq}$ and q_0 the stretch amplification before the onset of strain-induced crystallization. The mesoscopic stretch $\bar{\Lambda}$ is given by (see Appendix A)

$$\bar{\Lambda} = \left[\sum_{i=1}^{m} \frac{1}{m} \cdot \left((1 - w_i)\,\frac{I_1}{3} + w_i\Lambda_{\mathrm{i}}^2\right)\right]^{\frac{1}{2}}. \tag{16}$$

Since the representative strand contains only polymer chains in series, the tube diameters of the strand and a single chain are the same. Thus, the microscopic tube contraction is identical to the mesoscopic one and is given by (see Appendix A)

$$\bar{\upsilon} = \bar{\Upsilon} = \left[\sum_{i=1}^{m} \frac{1}{m} \left((1 - w_i)\,\frac{I_2}{3} + w_i\Upsilon_i^2\right)\right]^{\frac{1}{2}}. \tag{17}$$

Furthermore, due to the topological constraint, a polymer chain can only take part in the crystallization of either primary or secondary crystallite. Thus, the number of chains involved in the nucleation of the primary crystallite can be calculated as

$$N_{\mathrm{c}} = N_{\mathrm{c0}}\,(1 - \zeta_{\mathrm{c}})\,, \tag{18}$$

where N_{c0} is the total number of chains per unit reference volume of the rubber network, and $\zeta_c = 6\Phi\zeta_{\mathrm{II}}^{eq}$ is the fraction of misoriented chains.

The free energy of the equilibrium semi-crystalline network can be given by (Khiêm and

Itskov, 2018b)

$$\Psi^{eq} = U - T\eta = U_{\mathbf{F}}\left(\mathbf{F}, \Lambda_{\mathrm{i}}^{\mathrm{c}\,\max}\right) + c_0\left(T - T_0\right) - TN_{\mathrm{c}}s_{\mathbf{F}} - Tc_0 \ln\frac{T}{T_0}, \tag{19}$$

where T is the current (absolute) temperature, c_0 is the heat capacity per unit reference volume, $U_{\mathbf{F}}$ and $s_{\mathbf{F}}$ are the deformation-dependent part of the internal energy and entropy, respectively (see details in Appendix C).

The deformation-dependent part of the entropy $s_{\mathbf{F}}$ of a single chain is calculated as (Khiêm and Itskov, 2016)

$$s_{\mathbf{F}} = -k_{\mathrm{B}}n\kappa \ln\frac{\pi r}{n\sin\left(\dfrac{\pi r}{n}\right)} - k_{\mathrm{B}}\omega\bar{\upsilon}, \tag{20}$$

where ω is the tube parameter (Khiêm and Itskov, 2016) and $\bar{\upsilon} = \bar{\Upsilon}$ is the tube contraction (see details in Appendix A).

The end-to-end distance of the representative chain is given by (Khiêm and Itskov, 2018b)

$$r = \bar{\lambda}\sqrt{n} - \zeta_{\mathrm{b}}n. \tag{21}$$

As seen in Section 3, there is a change in crystal morphology from the primary to the secondary one during unloading. The change of $U_{\mathbf{F}}$ with respect to the alternation of crystal crystal morphology $\dfrac{\partial N_{\mathrm{c}}}{\partial \mathbf{F}}$ in the equilibrium network can be calculated as (Khiêm and Itskov, 2018b)

$$\frac{\partial U_{\mathbf{F}}}{\partial \mathbf{F}} = Ts_{\mathbf{F}}\frac{\partial N_{\mathrm{c}}}{\partial \mathbf{F}}. \tag{22}$$

4.2. Nonequilibrium semi-crystalline chains (free chains)

One can observe that the evolution of nonequilibrium crystallinity (10) represents a diffusion process of chain segments into nuclei. Thus, the internal energy due to the translational

motion of the chain segments can be given by

$$U_{\zeta}^{neq} = \frac{1}{2}\rho_c \hat{n}^2 l^2 \dot{\zeta}^2, \tag{23}$$

where ρ_c denotes the density of the polymer crystallite, $\hat{n}$ is the chain length of the free chain, l is the segment length, and $\hat{n}l\dot{\zeta}$ is the translational velocity of free chain segments. To the best of our knowledge, such definition of internal energy is unique and has not been postulated in the literature.

As mentioned in Section 3, the free chains are very long so that their entropic contribution is negligible. Thus, the semi-crystalline free energy reads as

$$\Psi = U - T\eta + U_{\zeta}^{neq}, \tag{24}$$

where the internal energy of equilibrium semi-crystalline chains $U = U_{\mathbf{F}} + c_0\,(T - T_0)$.

In view of (C.4), (22) and (24), the first Piola-Kirchhoff stress of the semi-crystalline network is given by

$$\mathbf{P}_{sc} = \mathbf{P}^{eq} + \mathbf{P}^{neq} = -TN_c \frac{\partial s_{\mathbf{F}}}{\partial \mathbf{F}} + \frac{\partial U_{\zeta}^{neq}}{\partial \mathbf{F}}. \tag{25}$$

Remark 2. *The previous equilibrium strain-induced crystallization theory (Khiêm and Itskov, 2018b) cannot reveal the existence of the internal energy* (23) *because in thermodynamic equilibrium* $\dot{\zeta} = 0$, (23) *vanishes. Furthermore, under dynamic loading, in view of* (23) *and* (11) *the term* $\mathbf{P}^{neq}$ *is positive indicating that the dynamic stress* $\mathbf{P}$ *is larger than the quasistatic stress* $\mathbf{P}^{eq}$*. This observation agrees well with experimental evidence (Brüning et al., 2012).*

5. Filler-polymer interaction

To describe the Mullins effect and rate-dependent effect in filled natural rubbers, the filler-interaction should be considered. Here, the rate-independent damage is captured by

an equilibrium filler-polymer network, while the rate-dependent effect is described by a nonequilibrium filler-polymer network.

5.1. Equilibrium filler-polymer network

For the sake of simplicity, the equilibrium filler-polymer network is derived from an isotropic damage-elastoplastic version (Khiêm and Itskov, 2017) of the Gent model (Gent, 1996). Its free energy function is given by

$$\Psi_f^{eq} = \delta\tilde{\mu}_c\,(1-n_m)\ln\left(1-\frac{\tilde{\lambda}-1}{n_m-1}\right)+(1-\delta)\tilde{\mu}_c\,(1-n_h)\ln\left(1-\frac{\tilde{\lambda}-1}{n_h-1}\right)+\tilde{\mu}_t\frac{I_2}{3}\sqrt{\frac{n_0}{n_m}}, \quad (26)$$

where $\tilde{\mu}_c$ is the phantom shear modulus and $\delta = 80\%$ is the initial fraction of irreversible damage Khiêm et al. (2021). Due to a low filler concentration, the microstretch of the filler-polymer network is obtained from an isotropic version of the analytical network averaging $\tilde{\lambda} = \dfrac{I_1}{3}$ (Khiêm and Itskov, 2016). More sophisticated approaches accounting for filler-polymer interaction can be found in Dargazany and Itskov (2009); Khiêm and Itskov (2017); Saadedine et al. (2021). n_m and n_h are the chain lengths corresponding to irreversible and reversible disentanglements of polymer chains from filler surface, respectively. Due to such disentanglements, n_m and n_h will increases during deformation in a similar manner as the network alteration model (Marckmann et al., 2002)

$$n_m = n_0 + \alpha(\tilde{\lambda}^{\max} - 1), \quad (27)$$

$$n_h = n_0 + \alpha(\tilde{\lambda}^{c\max} - 1), \quad (28)$$

where n_0 is the initial chain length, $\tilde{\lambda}^{\max}$ and $\tilde{\lambda}^{c\max}$ are internal variables which will be defined below. $\alpha > 0$ is a material parameter representing the relative number of chain segments disentangled from the filler surface by deformation.

To describe multiple cycles of damage in filled natural rubbers, we extend the analytical perfect elastoplastic theory (Khiêm and Itskov, 2017) by including an isotropic hardening law (see details in Appendix D). Accordingly, the value of the internal variable will be

updated at the beginning of every new loading cycle as

$$\tilde{\lambda}^{c\max} = \max_{\tau\in\left[t_{\mathrm{i}}^{c},t\right]} \tilde{\lambda}(\tau), \tag{29}$$

$$\tilde{\lambda}^{\max}(t) = \beta^{c-1} \max_{\tau\in[-\infty,t]} \tilde{\lambda}(\tau), \tag{30}$$

where the ending time of the c^{th} loading cycle t_{i}^{c} is defined by the local minimum of $\tilde{\lambda}$ within the time interval $\tau \in (-\infty, t]$. β is a parameter describing the irreversibility of the disentanglement. In the example considered here, $\beta = 1.2$ and $\max(c) = 3$ since the material is stabilized after 3 cycles of loading (Khiêm et al., 2021).

5.2. Nonequilibrium filler-polymer network

The nonequilibrium filler-polymer network is obtained on the basis of stretch multiplicative decomposition (Reese and Govindjee, 1998; Dal et al., 2020). Accordingly, the microscopic stretch applied on polymer strand is decomposed into elastic and viscous part $\tilde{\lambda} = \tilde{\lambda}^{e}\tilde{\lambda}^{v}$. The physical motivation for such multiplicative decomposition could be a diffusion of chain segments through entanglements (Dal et al., 2020). The flow rule for the rate-dependent internal variable $\tilde{\lambda}^{v}$ is given by

$$\dot{\tilde{\lambda}}^{v} = \frac{1}{\tau_f} \frac{\partial \Psi_f^{neq}\left(\tilde{\lambda}^{e}\right)}{\partial \tilde{\lambda}^{e}}, \tag{31}$$

where τ_f is the relaxation time. The nonequilibrium free energy of the filler-polymer network is given by

$$\Psi_f^{neq} = \hat{\mu}\,(1-n_0)\ln\left(1 - \frac{\tilde{\lambda}^{e}-1}{n-1}\right). \tag{32}$$

Equation (32) expresses therefore the free energy of the nonequilibrium branch of the rheological model with the stretch $\tilde{\lambda}^{e}$.

6. Constitutive formulation

6.1. Total free energy

The total free energy is a summation of entropic and energetic contribution from the semi-crystalline chains and filler-polymer interaction. Thus, in view of (24), (23), (26) and (32), the total free energy of filled natural rubbers takes the form

$$\Psi_{total} = U - T\eta + U_{\zeta}^{neq} + \Psi_{f}^{eq} + \Psi_{f}^{neq}. \tag{33}$$

The total first Piola-Kirchhoff stress tensor is therefore given by

$$\mathbf{P}_{total} = -TN_c \frac{\partial s_{\mathbf{F}}}{\partial \mathbf{F}} + \frac{\partial U_{\zeta}^{neq}}{\partial \mathbf{F}} + \frac{\partial \Psi_{f}^{eq}}{\partial \mathbf{F}} + \frac{\partial \Psi_{f}^{neq}}{\partial \mathbf{F}} - p\mathbf{F}^{-\mathrm{T}}, \tag{34}$$

where p is a Lagrange multiplier due to the incompressibility constraint. For readers convenience, the material parameters of the model and their physical meaning are listed in Table 1.

Table 1: Physical meaning of the material constants

Parameters	Physical meaning
$\mu_{\mathrm{c}} = N_{\mathrm{c}0} k_{\mathrm{B}} T_0 \kappa$	Effective phantom shear modulus at the room temperature [MPa]
n	Semi-crystalline chain length
q_0	Stretch amplification exponent at the room temperature
$\mu_{\mathrm{t}} = N_{\mathrm{c}0} k_{\mathrm{B}} T_0 \omega$	Topological shear modulus at the room temperature [MPa]
χ	Relative ratio of surface tension
B_1	Primary crystallinity constant
B_2	Secondary crystallinity constant
τ_n	Characteristic time of nonequilibrium crystallization [s]
$\rho_c \hat{n}^2 l^2$	Free chain inertia [s^{2}MPa]
$\tilde{\mu}_c$	Equilibrium phantom shear modulus of the filler-polymer network [MPa]
α	Relative number of disentangled segments.
n_0	Filler-polymer chain length
$\tilde{\mu}_t$	Equilibrium topological shear modulus of the filler-polymer network [MPa]
$\hat{\mu}$	Nonequilibrium shear modulus of the filler-polymer network [MPa]
τ_f	Relaxation time [s]

Note that in comparison to the equilibrium crystallization theory (Khiêm and Itskov, 2018b), only two new parameters τ_n and $\rho_c\hat{n}^2l^2$ were introduced to characterize the nonequilibrium crystallization response. The last six material parameters in Table 1 are related to equilibrium and nonequilibrium filler-polymer interaction.

6.2. Thermodynamic consitency

The model includes four types of internal variables. The equilibrium internal variables $\tilde{\lambda}^{\max}$ (and $\tilde{\lambda}^{c\max}$) describe the rate-independent damage-elastoplasticity, $\bar{\Lambda}_{\mathrm{i}}^{\mathrm{c}\max}$ is essential for the description of equilibrium crystallization under unloading, whereas the nonequilibrium internal variables are the nonequilibrium crystallinity ζ and the viscous stretch $\tilde{\lambda}^{v}$ describing the rate-dependent filler-polymer interaction. Therefore, the total instrinsic dissipation contains four parts as

$$D_{total} = D^{eq} + D_f^{eq} + D_\zeta^{neq} + D_f^{neq}. \tag{35}$$

The dissipation due to equilibrium crystallization reads as

$$D^{eq} = \sum_{i=1}^{m}\left(-\frac{\partial U_{\mathbf{F}}}{\partial \Lambda_{\mathrm{i}}^{\mathrm{c}\max}}\dot{\Lambda}_{\mathrm{i}}^{\mathrm{c}\max} + T s_{\mathbf{F}}\frac{\partial N_{\mathrm{c}}}{\partial \Lambda_{\mathrm{i}}^{\mathrm{c}\max}}\dot{\Lambda}_{\mathrm{i}}^{\mathrm{c}\max}\right) = 0. \tag{36}$$

The elastoplastic dissipation can be expressed as

$$D_f^{eq} = -\frac{\partial \Psi_f^{eq}}{\partial \tilde{\lambda}^{\max}}\dot{\tilde{\lambda}}^{\max} - \frac{\partial \Psi_f^{eq}}{\partial \tilde{\lambda}^{c\max}}\dot{\tilde{\lambda}}^{c\max} = \delta\left(f\left(n_m\right) + \frac{\tilde{\mu}_t I_2\sqrt{n_0}}{6n_m^{3/2}}\right)\alpha\dot{\tilde{\lambda}}^{\max} + (1-\delta) f\left(n_h\right)\alpha\dot{\tilde{\lambda}}^{c\max} \geq 0, \tag{37}$$

since during loading $f\left(x\right) = \tilde{\mu}_c\left(\frac{\tilde{\lambda}-1}{x-\tilde{\lambda}} + \ln\left(1-\frac{\tilde{\lambda}-1}{x-1}\right)\right) > 0$, $\dot{\tilde{\lambda}}^{\max} > 0$ and $\dot{\tilde{\lambda}}^{c\max} > 0$, whereas under unloading $\dot{\tilde{\lambda}}^{\max} = 0$ and $\dot{\tilde{\lambda}}^{c\max} = 0$.

In view of (10) and (23), the dissipation due to nonequilibrium crystallization reads

$$D_\zeta^{neq} = \frac{\rho_c\hat{n}^2l^2\dot{\zeta}^2}{\tau_n} > 0. \tag{38}$$

As a result of (31) and (32), the dissipation in the nonequilibrium filler-polymer network

$$D_f^{neq} = -\frac{\partial \Psi_f^{neq}}{\partial \tilde{\lambda}^v}\dot{\tilde{\lambda}}^v = \frac{\tilde{\lambda}\tau_f}{\left(\tilde{\lambda}^v\right)^2}\left(\dot{\tilde{\lambda}}^v\right)^2 \tag{39}$$

is always positive. Thus, in view of (36), (37), (38) and (39), $D_{total} > 0$. The proposed model always satisfies the second law of thermodynamics.

7. Results

7.1. Uniaxial tension of filled natural rubber

In this section, parameters of the developed constitutive model are determined by comparison with multiple cyclic loading experimental data in uniaxial tension of a filled natural rubber (Khiêm et al., 2021). This experimental data set is obtained from four tests: pure cyclic loading of the sample (I), cyclic loading with relaxation (II), preconditioning test (IIIa) and preconditioning with relaxation (IIIb). All the tests were performed with the same filled natural rubber and at the same stretch rate. The volume fraction of filler in this natural rubber is $w_0 = 0.1$, the surface tension production of bundle-like crystallite $\gamma_t\gamma_s^2 = 1.39e-11[J^3m^{-6}]$ (cf. Gros et al. (2015)), and the experiment was carried out at room temperature $T_0 = 295[K]$. For the sake of simplicity, a version of (A.1) with $m = 3$ is used in this section. Here, the stress-stretch and crystallinity measured in (II) and (IIIa) will be used for model fitting, while the mechanical behavior in (I) and (IIIb), heat source and temperature variation of all tests are utilized to verify the predictive capability of the model. To this end, the parameters of the filler-polymer network $\tilde{\mu}_{c,t}$, α, n_0 and $\hat{\mu}$ are first obtained from the fitting to cyclic loading (II) up to stretch 2.5, below which strain-induced crystallization does not occur. To determine the relaxation time of filler-polymer interaction τ_f, the model was fitted to the relaxation test (II) at stretch 2.5. Finally, by fixing the above mentioned material constants, the parameters for the semi-crystalline network (the first 9 parameters in Table 1) can be obtained by simultaneous fitting to the experimental crystallinity from the infrared thermography based quantitative surface calorimetry and the

stabilized cycle of the stress-stretch response of preconditioning test (IIIa). The so obtained material parameters are listed in Table 2.

7.1.1. Stress-stretch behavior

The mechanical responses of the model in the four tests are demonstrated in Figure 4 versus the corresponding experimental data. As mentioned above, the model was fitted only to the experimental data in Figure 4*b* and *c*. It can be seen that the model demonstrates good agreement with experimental data with respect to the Mullins effect, hysteresis and stress relaxation under both loading and unloading (see Figure 5). Note that the model can also describe the permanent set resulting from the rate-dependent response of the filler-polymer interaction (32). Special attention is focused on stress relaxation at $\Lambda = 2.5$, $\Lambda = 4$ and $\Lambda = 6$ (Figure 5*b* and *d*). Since the onset of strain induced crystallization takes place at stretch larger than $\Lambda_1 = 2.5$, the first stress relaxation is purely due to the viscoelasticity of filler-polymer interaction (32). At higher stretch ratios, the stress relaxation is due to both the viscoelasticity of filler-polymer interaction and the reduction of diffusion velocity of crystalline segments (10) in free chains. These effects will be analyzed further in the crystallinity analysis.

7.1.2. Crystallinity

The total crystallinities predicted by the model are demonstrated in Figure 6 versus experimental data. There, only the loading branch in Figure 6*c* was fitted to the experimental data, while all remaining curves are pure model predictions. It can be seen that the onset of strain-induced crystallization for the specific filled natural rubber is at $\Lambda_c = 3.5$. It is earlier than that of unfilled natural rubber ($\Lambda_c = 4$) due to the strain amplification effect (Rault

Table 2: Material constants of the proposed model for the filled natural rubber in Khiêm et al. (2021).

μ_c[MPa]	n	q_0	μ_t[MPa]	χ	B_1	B_2	$\tau_n[s]$	$\rho_c\hat{n}^2l^2[s^2\text{MPa}]$
0.1484	16.313	0.9276	0.3410	2	0.7	0.859	25	1e5
$\tilde{\mu}_c$[MPa]	α	n_0	$\tilde{\mu}_t$[MPa]	$\hat{\mu}$[MPa]	$\tau_f[s]$			
0.1389	1.02	1.2718	0.05	0.9	60			

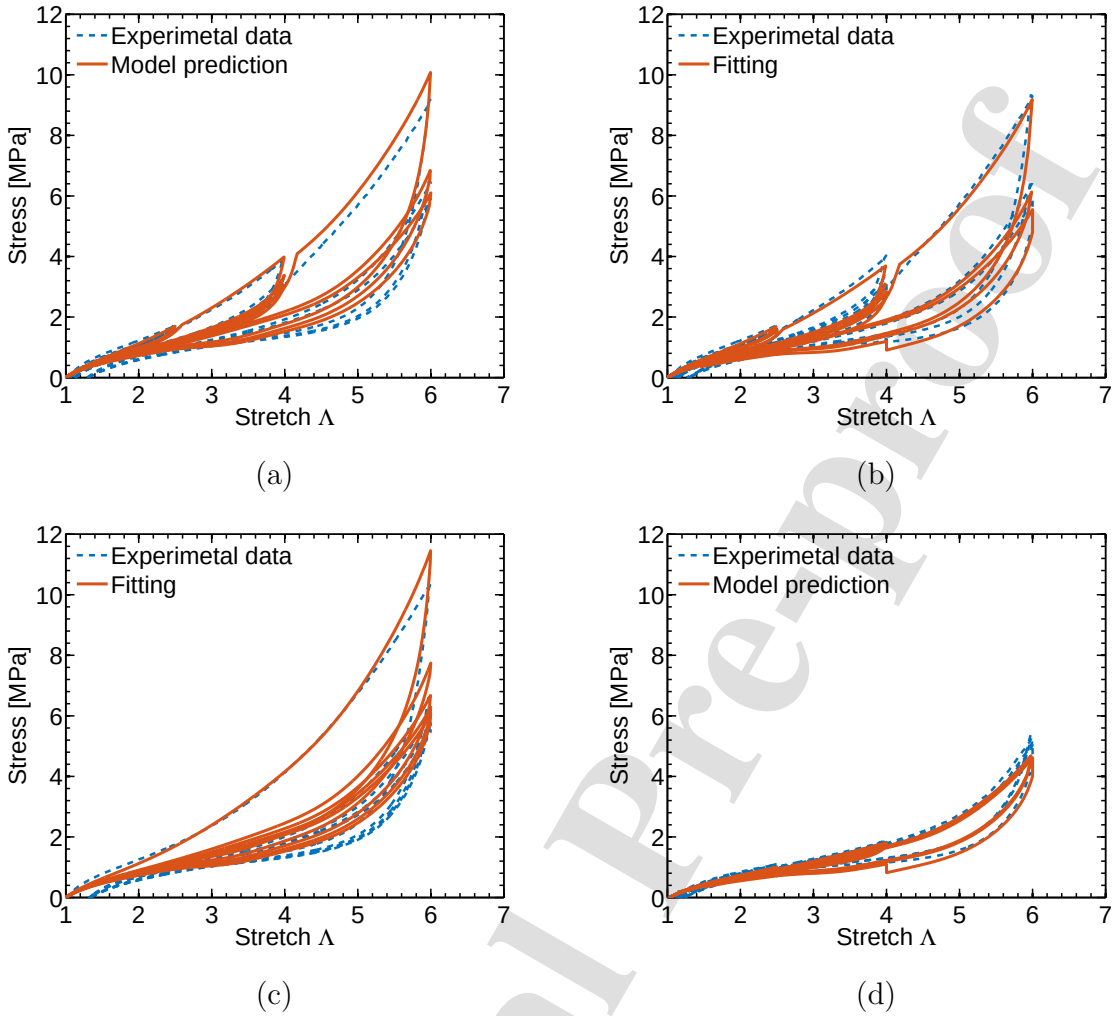

Figure 4: Stress vs. stretch predicted by the proposed model in the four situations: (a) Cyclic loading without preconditioning; (b) Cyclic relaxation without preconditioning; (c) Preconditioning step; (d) Cyclic relaxation after preconditioning.

et al., 2006b), and this effect is captured in the model via (1). Furthermore, the crystallinity in the loading branch of all testing situations is approximately the same (i.e. up to 14%). However, the behaviors under unloading and especially when stress relaxation takes place deviate strongly from the quasi-static (equilibrium) situation (Khiêm and Itskov, 2018b). First, it is observed that not all crystallites melt under unloading, which is indicated by a permanent crystallity $\approx 1\%$ at the end of unloading (Figure 6). Second, the stress relaxation seems to promote the development of new crystallites, as an increase of crystallinity can be

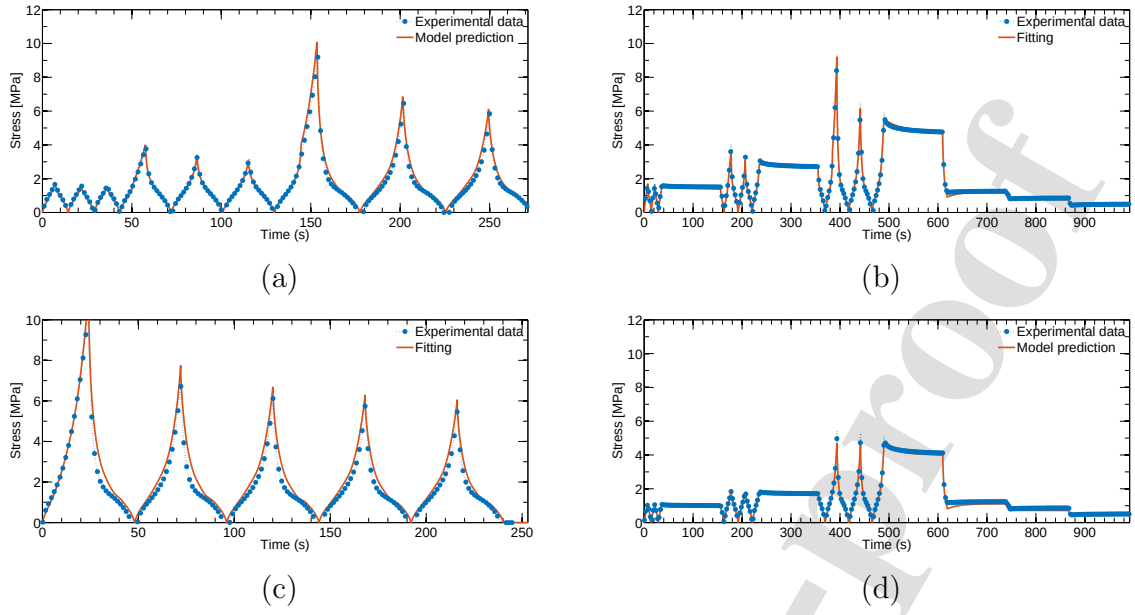

Figure 5: Stress vs. time predicted by the proposed model in four situations: (a) Cyclic loading without preconditioning; (b) Cyclic relaxation without preconditioning; (c) Preconditioning step; (d) Cyclic relaxation after preconditioning.

seen during the stress relaxation at $\Lambda = 6$ (Figure 6*b* and *d*).

Remark 3. *In the unloading case, two types (primary and secondary) of crystallite occur in the rubber network. Since those crystallites have different melting rates (indicated by* (3) *and* (6)*), the unloading curve of the crystallinity is non-monotonic. The branch before the kink in Figure 6 is dominated by the melting of the primary crystallites, while the one afterwards represents the melting of the secondary crystallites.*

To understand better the evolution of crystallinity under dynamic loading, especially in stress relaxation, the equilibrium and nonequilibrium parts of the crystallinity are plotted versus time in two loading scenarios (I) cyclic loading without stress relaxation and (II) cyclic loading with stress relaxation (Figure 7). One observes that there is no nonequilibrium crystallinity during the stress relaxation at the stretch below the onset of strain-induced crystallization (from 40-160s). Conversely, the tertiary crystallinity grows from the primary nuclei during the relaxation at stretch 4 (from 220-380s) and stretch 6 (from 490-605s) in Figure 7*b*, since the crystal nuclei already occur before (at $\Lambda_c = 3.5$). This leads to higher total crystallinity at $\Lambda = 4$ in the test with relaxation, in comparison to the nonrelaxation one

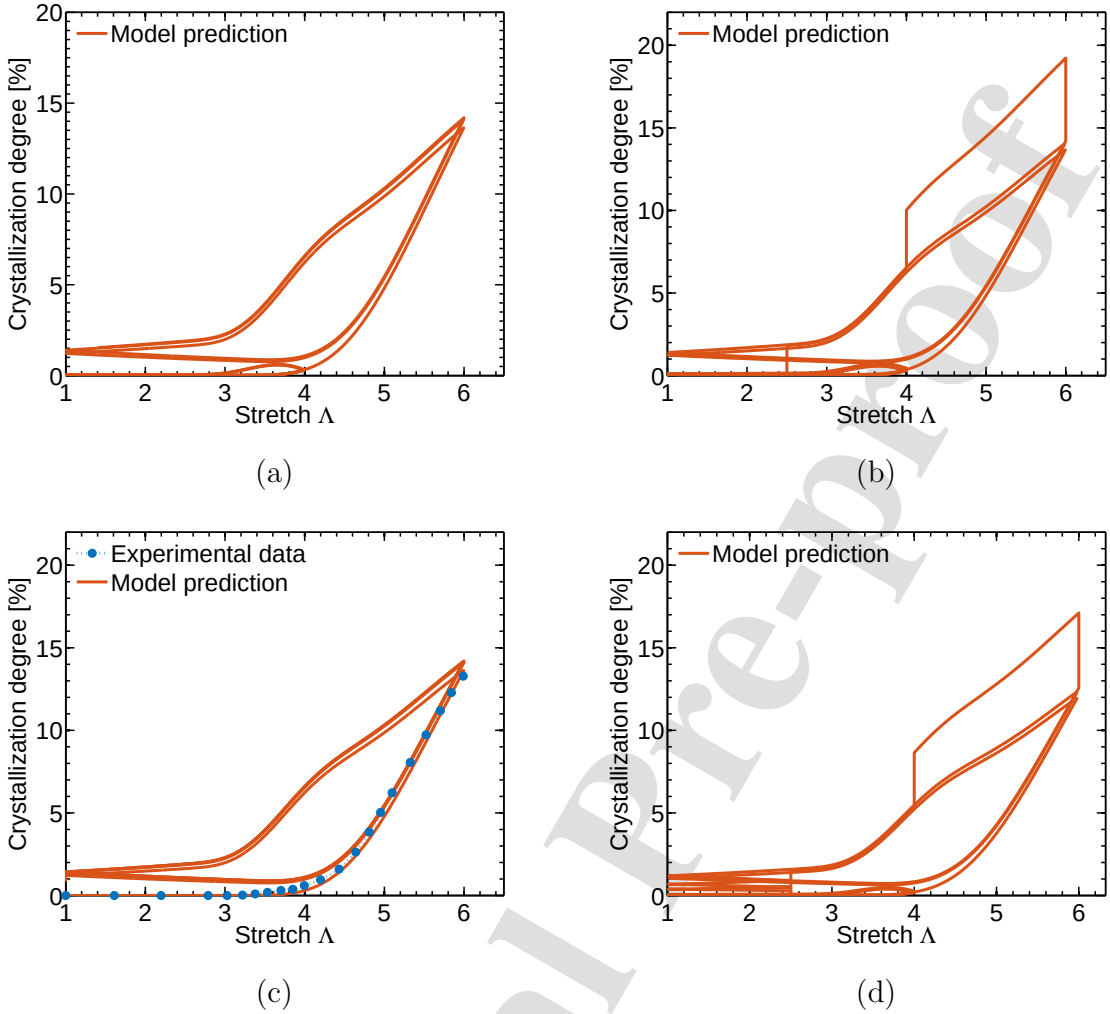

Figure 6: Total crystallinity predicted by the proposed model in four situations: (a) Cyclic loading without preconditioning; (b) Cyclic relaxation without preconditioning; (c) Preconditioning step; (d) Cyclic relaxation after preconditioning.

(Figure 7*a*). Furthermore, both the nucleation and melting rates of equilibrium crystallites are significantly higher than those of the nonequilibrium ones. The residual crystallinity is only due to nonequilibrium crystallization, which is clearly depicted in Figure 7*a* at 190s, 238s and 291s, and in Figure 7*b* at 405s and 460s. More specifically, since the melting of nonequilibrium crystallites is much slower than that of the equilibrium one (Figure 7), the residual crystallites will be nonzero if the non-stretching time (i.e. the duration of unloading or stress relaxation) is insufficient. At the relaxation at stretch $\Lambda_1 = 6$, the growth of tertiary

crystallites is tremendous (as shown by the nonequilibrium crystallinity ζ in Figure 7*b*) since the number of nuclei is high (about 14%, see Figure 6*b*). Thus, the kinetics of nonequilibrium crystallinity favors stress relaxation during loading. This observation can be easily verified by recalling the solution of nonequilibrium crystallinity evolution (10). Due to the growth of tertiary crystallites, the magnitude of nonequilibrium crystallinity is significantly larger than during pure loading (cf. (11) and (12)). During the stress relaxations under unloading (600-720s) and (745-865s) there is a competition between the growth of tertiary crystallites and the melting of their nuclei (in non-stretching situation, Figure 2). In contrast to the situation under pure cyclic loading (I), all crystallites can melt at the end of the experiment (II) since the stress relaxation lengthens the total non-stretching time, see Figure 7*b*.

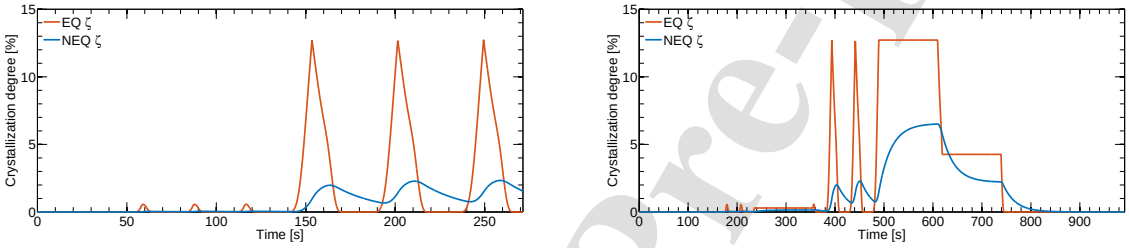

Figure 7: Time evolution of equilibrium and nonequilibrium crystallinity in two loading scenarios: (a) Cyclic loading without preconditioning; (b) Cyclic relaxation without preconditioning.

7.1.3. Local heat source

In view of (33) and (C.10), the local heat source for filled natural rubbers can be decomposed as

$$\hat{S} = \left(\mathbf{P} - \frac{\partial U_{\mathbf{F}}}{\partial \mathbf{F}} - \frac{\partial U_{\zeta}^{neq}}{\partial \mathbf{F}} \right) : \dot{\mathbf{F}} + D_{\zeta}^{neq} + \Delta H \dot{\zeta}^{total}. \tag{40}$$

The first term in (40) represents the entropic power, the second term is the intrinsic dissipation due to nonequilibrium crystallization, and the last term is the internal heat supply due to phase transition.

To justify the prediction of crystallinity under unloading and stress relaxation, the local heat source calculated by the model (40) is depicted in Figure 8. The evolution of heat

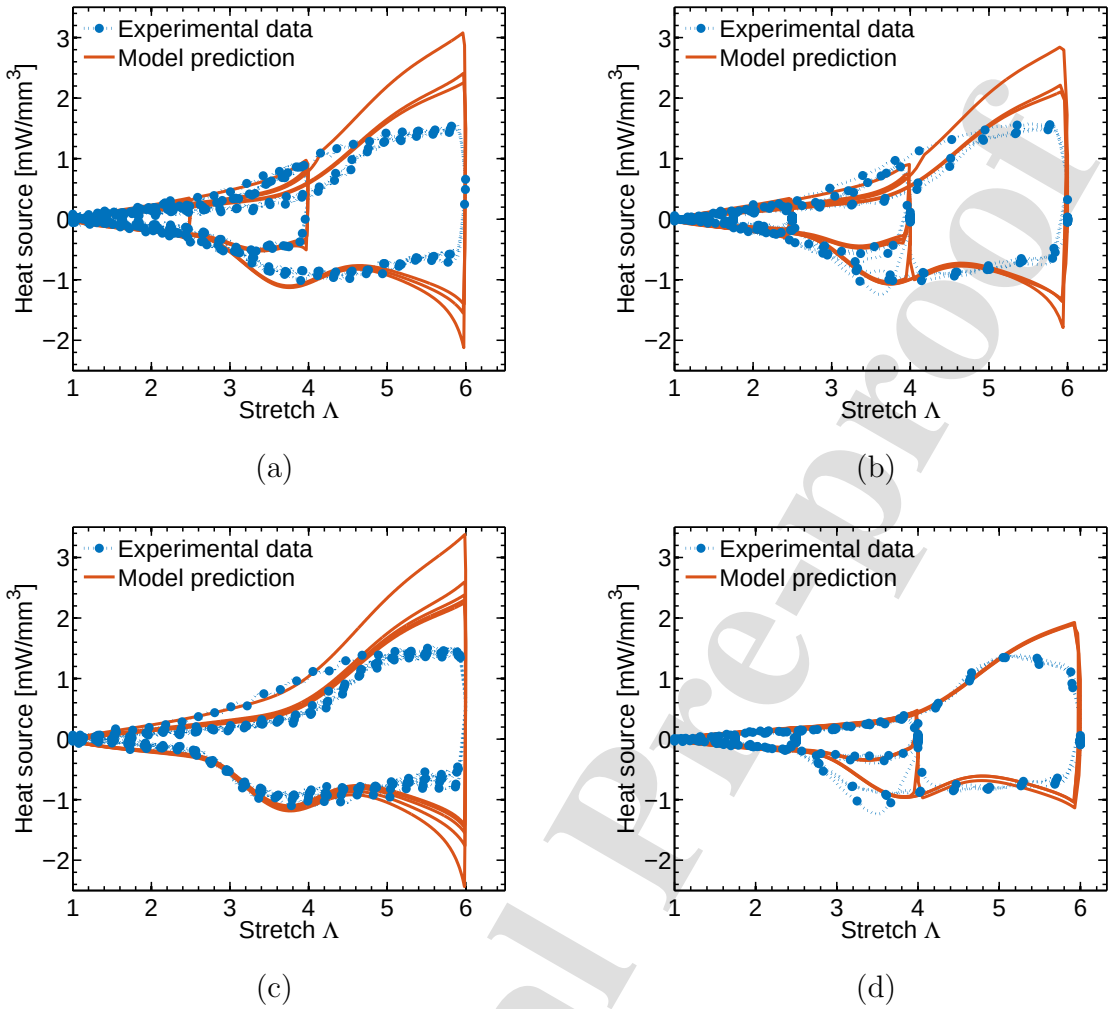

Figure 8: Local heat source vs. stretch predicted by the proposed model in the four situations: (a) Cyclic loading without preconditioning; (b) Cyclic relaxation without preconditioning; (c) Preconditioning step; (d) Cyclic relaxation after preconditioning.

source before the crystallization starts can be well captured. It can be seen that the upturn (during loading) and downturn (during unloading) of the heat source are correctly predicted by the model in all loading situations. Thus the predicted onset of crystallization ($\Lambda_c = 3$) and the equilibrium melting point ($\Lambda_m = 2.5$) are accurate. Nevertheless, the model always overestimate the local heat source after the onset of crystallization. It is due to the omission of an energetic contribution of crystallinity under loading (Section 4). The model can also reproduce the variation of heat source between different loading cycles. Accordingly, due to

the Mullins effect, the heat production in the virgin loading is significantly higher than that in the subsequent loading. It is in good agreement with the discussion in Part I (Khiêm et al., 2021). One should note that the heat absorption at stretch $\Lambda = 4$ after the stress relaxation (Figure 8*b* and *d*) is much stronger than that in the test without relaxation (Figure 8*a*), and such effect does not appear at stretch $\Lambda = 6$. Thus, the evolution of crystallization after stress relaxation (Khiêm et al., 2021) at two stretches $\Lambda = 4$ and $\Lambda = 6$ appears to be different.

To reveal the origin of the change in heat source during such deformation, the three contributions of the local heat source (40) should be analyzed. It can be easily seen that the dissipation due to unequilibrium crystallization is always positive, however its magnitude is almost zero due to a very slow rate of unequilibrium crystallization ($\tau_n = 25s$) in (38). Furthermore, such dissipation is related to heat production (positive) so it cannot explain the heat absorption (negative). Thus only two significant contributions of the local heat source, the entropic power and the internal heat supply are plotted in two loading scenarios: cyclic loading without (I) and with stress relaxation (II) (Figure 9).

It can be seen that the entropic contribution of heat source in both cases are more or less the same. Thus, the deviation in the heat absorption at the stretch $\Lambda = 4$ between the two experiments (I) and (II) is solely due to the difference in internal heat supply (see Figure 9*b* and *d*). It can be explained by an increase of equilibrium crystallinity at the beginning of unloading (around time 355s) after the stress relaxation at $\Lambda = 4$ in Figure 7*b*. It is due to the fact that at stretch $\Lambda = 4$, the attachment of chain segments on the nuclei surface (B.8) is faster than the melting of the nuclei (B.7). Furthermore, such increase in equilibrium crystallinity is not observed after the stress relaxation at $\Lambda = 6$ (around time 600s) because at higher stretch the melting of the nuclei is faster and hinder crystallization growth. Note that although there is a large nonequilibrium crystallinity (about 5%) during stress relaxation at $\Lambda = 6$, its rate is much slower than that of equlibrium crystallinity (Figure 7*b*), so the contribution of nonequilibrium crystallinity to the heat source at $\Lambda = 6$ is insignificant.

Finally, it is observed that during last phases of stress relaxation (from time 490s),

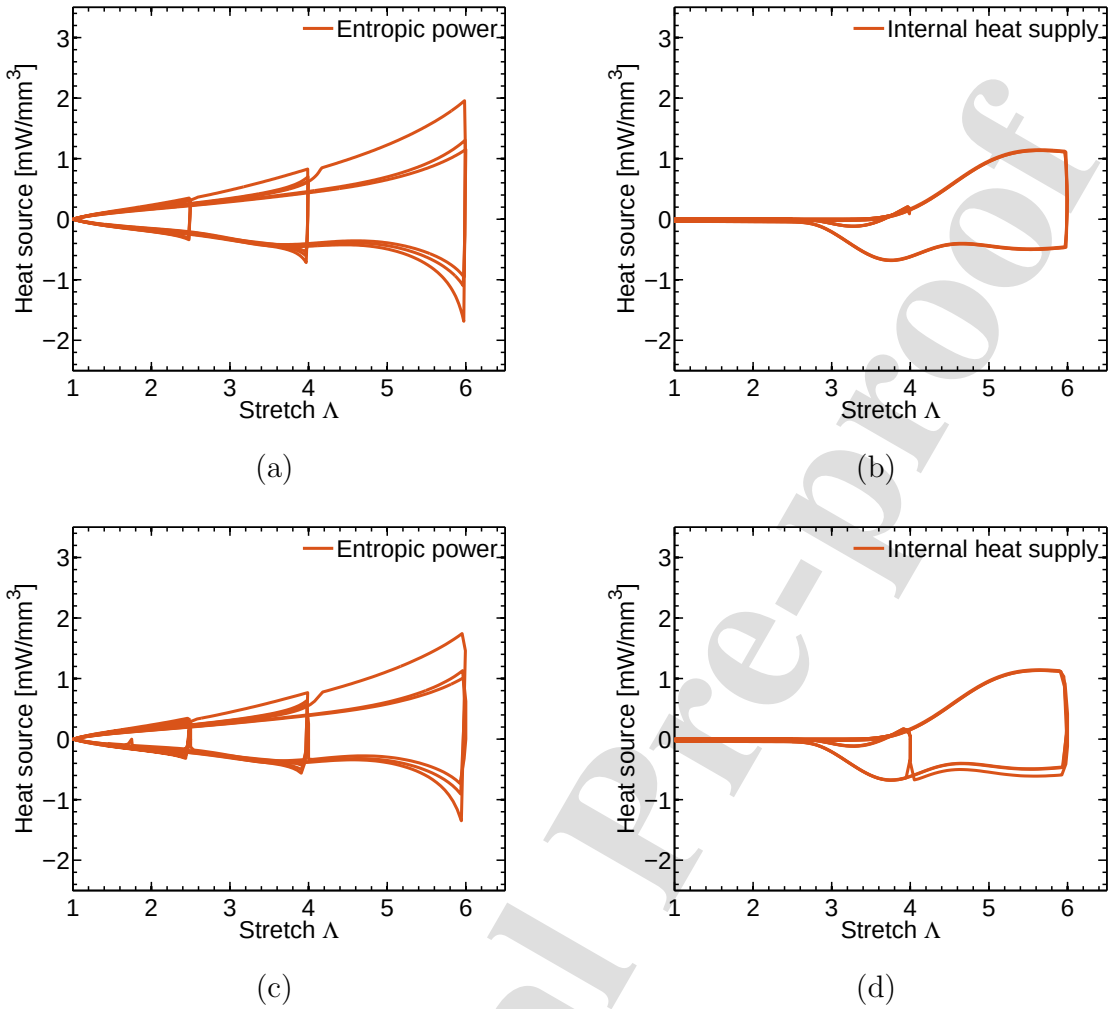

Figure 9: Two contributions of the local heat source predicted by the proposed model in two loading situations: (a,b) Cyclic loading without stress relaxation; (c,d) Cyclic loading with stress relaxation.

the heat production remains strictly positive throughout the relaxation time (490-605s), while the heat absorption under the unloading remains strictly negative until the end of the unloading (Figure 10). It is due to the appearance of nonequilibrium crystallites in stress relaxation phases (Figure 7*b*), which prevent the internal heat supply from returning to zero. At the end of unloading in the experiment (II), all crystallites melt so that the heat absorption returns to zero. As seen in Figure 10*b*, the internal heat supply due to phase transition plays a major role in the change of heat absorption of natural rubber, especially during the stress relaxation.

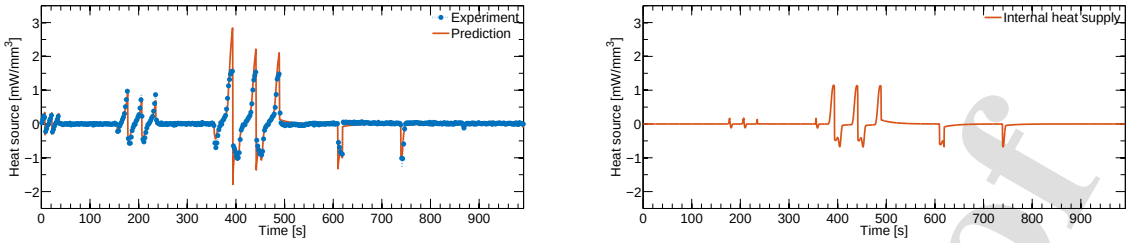

(a) (b)

Figure 10: Time evolution of local heat source during the cyclic loading with relaxation: (a) Total heat source; (b) Internal heat supply.

7.1.4. Temperature variation of filled natural rubbers in uniaxial tension

For the sake of simplicity, the specimen temperature was determined from an 1D thermal diffusion problem to predict the calorimetric response. We assume that the deformation of specimen is homogeneous, and there is only a variation of temperature along the thickness direction X_3. This assumption is realistic since thin specimens were used in the experiment (Khiêm et al., 2021).

In this situation, (C.9) can be simplified as

$$c_0\dot{T}\left(X_3,t\right)=k_0\frac{1}{\Lambda_3^2}\frac{\partial^2 T}{\partial X_3\partial X_3}+P_1\dot{\Lambda}_1-\dot{U}_{\mathbf{F}}-\dot{U}_{\zeta}^{neq}+\Delta H\dot{\zeta}^{total}. \tag{41}$$

The thermal conductivity of natural rubber is $k_0 = 0.2[\frac{mW}{mmK}]$ and the heat capacity per unit reference volume $c_0 = 1.645[\frac{mJ}{mm^3K}]$, the latent heat of fusion $\Delta H = 59.9(1-w_0)[\frac{mJ}{mm^3}]$ (Khiêm et al., 2021).

In uniaxial tension, the thinner the sample, the more efficient the heat transfer to the environment is. Thus, the film coefficient of natural rubber to the air is assumed proportional to the change of sample thickness, $\hat{h} = h_0{\Lambda_3}^{-1}$, where h_0 is the initial film coefficient. By Nanson's formula, the Lagrangian version of the convection boundary condition reads as

$$h_0{\Lambda_3}^{-1}\cdot\left(T(X_3,t)-T_0\right)=-k_0\Lambda_3^{-1}\frac{\partial T(X_3,t)}{\partial X_3},\qquad \text{on } X_3=\frac{H}{2}, \tag{42}$$

where $H = 2[mm]$ is the thickness of the sample and $h_0 = 0.0174[\frac{mW}{mm^2K}]$ (Sae-oui et al.,

1999). A symmetric boundary condition is applied at the center of the specimen ($X_3 = 0$) due the the symmetry of the temperature distribution. Given the initial condition

$$T\left(X_3, 0\right) = T_0, \qquad \forall X_3 \in \left[0, \frac{H}{2}\right], \tag{43}$$

the partial differential equation (41) can be solved for $T\left(X_3, t\right)$ using the finite difference method. The average temperature change can be calculated as

$$\theta\left(t\right) = \frac{2}{H} \int_0^{\frac{H}{2}} T\left(X_3, t\right) dX_3 - T_0, \tag{44}$$

where $T_0 = 295[K]$ in the uniaxial tension test.

The average temperature variations (44) predicted by the model in the four tests are plotted in Figure 11. One observes very good agreement between the model prediction and experimental data. It is easily seen that the thermodynamic process is non-adiabatic. There is a discrepancy between the temperature variation predicted by the model and the experimental data during the relaxation phase of Figure 11*d*, since a very simple viscoelastic model was used for the nonequilibrium branch of the filler-polymer interaction (32). Furthermore, the temperature variation under the stress relaxation is very sensitive to the magnitude of the heat source, a slight difference in the predicted heat source can lead to such deviation in the temperature.

7.2. Validation and prediction of the model in biaxial tension

In this section, to further study the model, its predictions of heat source, crystallinity and temperature variation in a biaxial tension test (Part I - Khiêm et al. (2021)) are evaluated at the center of the specimen.

To this end, the local heat source is calculated as

$$\hat{S} = P_1 \dot{\Lambda}_1 + P_2 \dot{\Lambda}_2 - \dot{U}_{\mathbf{F}} - \dot{U}_{\zeta}^{neq} + \Delta H \dot{\zeta}^{total}, \tag{45}$$

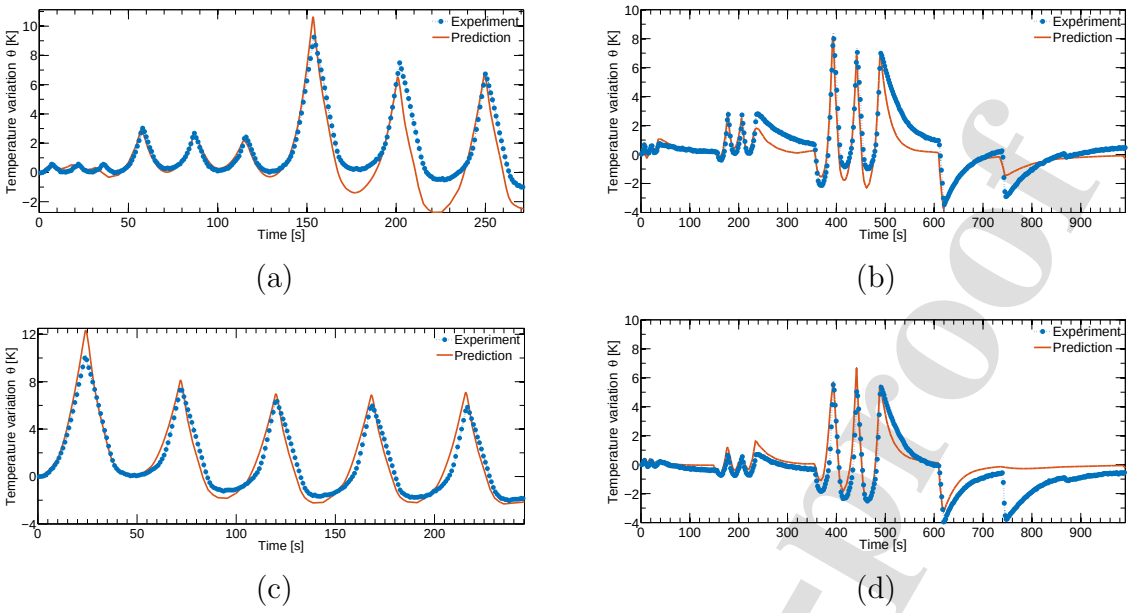

Figure 11: Time evolution of temperature variation predicted by the proposed model in four situations: (a) Cyclic loading without preconditioning; (b) Cyclic relaxation without preconditioning; (c) Preconditioning step; (d) Cyclic relaxation after preconditioning.

where the latent heat of fusion is assumed independent of the deformation state (Khiêm et al., 2021).

The predicted heat source (45) is plotted in Figure 12. To reduce the noise, a smoothing algorithm was applied on the measured deformation field (Figure 13*b*). In contrast to the uniaxial tension result, very good agreement between model prediction and experimentally measured values can be observed, both in the virgin loading and the subsequent cycles. It is due to the fact that the deformation is in the vicinity of onset of strain-induced crystallization ($\Lambda \approx \Lambda_c^{BT} = 3$), the crystallinity is small so that the energetic contribution of crystallinity (Section 4) is negligible. It can be seen that the heat source after the second loading cycle is significantly lower than that of the first cycle. It is due to the Mullins effect and a large amount of crystallinity disappears in the subsequent cycles due to lower maximum values of principal stretches (Figure 13*b*). It turns out that the crystallization is very sensitive in this specific biaxial tension, since in the vicinity of the crystallization onset, a small change in stretch leads to a significant change in the crystallinity. These effects can be seen in the plot of predicted crystallinity (Figure 13). Furthermore, it can be seen that the heat

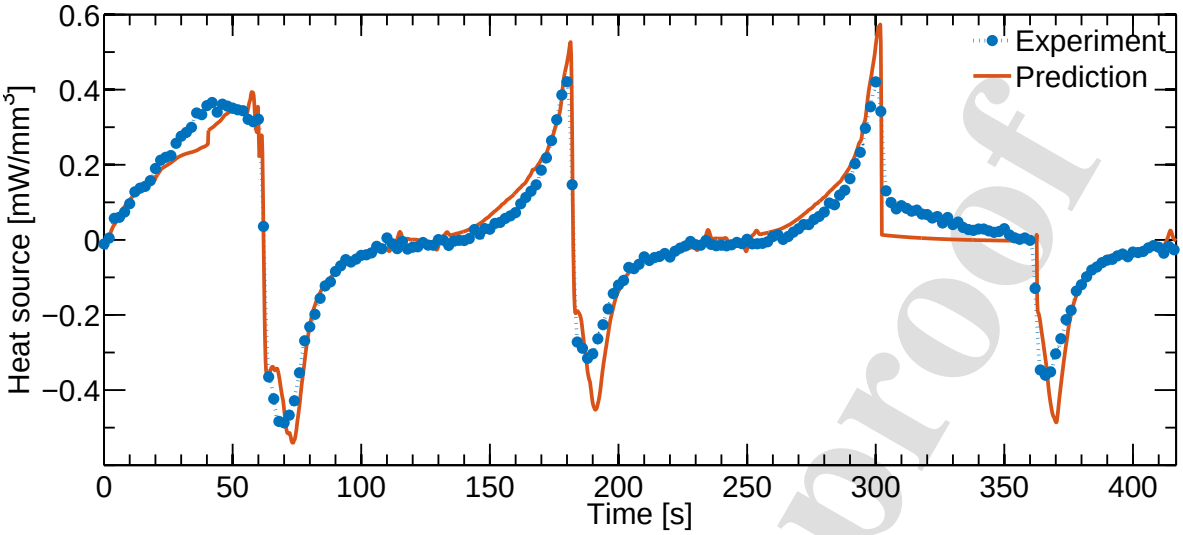

Figure 12: Average heat source predicted by the model in biaxial tension.

source during the constant displacement phase (301-361s, see details in Part I - Khiêm et al. (2021)) is positive (Figure 12). It is due to the growth of tertiary crystallites, which can be revealed in the crystallinity-stretch plot (Figure 14*b*). Furthermore, it should be noted that the crystallinity experimentally detected by the infrared thermography based quantitative surface calorimetry was evaluated using the second loading curve, therefore good agreement between the predicted crystallinity and the experimental data can be only observed on the second cycle. The maximal crystallinity in this case is about 2%. For the first cycle, the model predicts higher value of crystallinity since the principal stretches are higher there (Figure 13*b*).

The heat diffusion equation for the biaxial tension takes the form

$$c_0\dot{T}\left(X_3,t\right)=k_0\frac{1}{\Lambda_3^2}\frac{\partial^2 T}{\partial X_3}+P_1\dot{\Lambda}_1+P_2\dot{\Lambda}_2-\dot{U}_{\mathbf{F}}-\dot{U}_{\zeta}^{neq}+\Delta H\dot{\zeta}^{total}. \tag{46}$$

As the biaxial tension was carried out from the initial temperature $T_0=300[K]$, the film

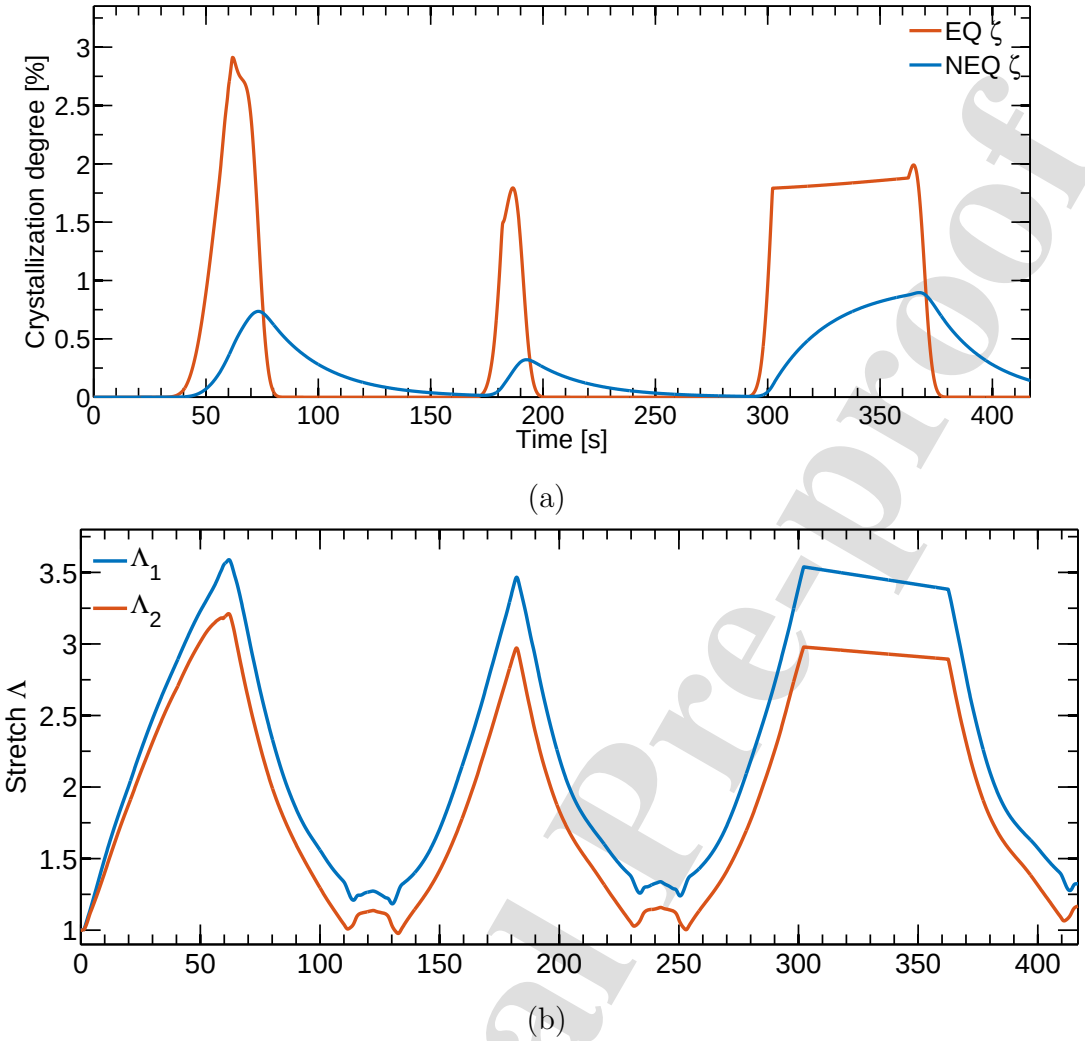

Figure 13: Crystallinity predicted by the model (a) under the (smoothed) deformation history (b).

coefficient is assumed to be h_0, the convection boundary condition reads as

$$h_0 \cdot (T(X_3,t) - T_0) = -k_0 \Lambda_3^{-1} \frac{\partial T(X_3,t)}{\partial X_3}, \qquad \text{on } X_3 = \frac{H}{2}. \tag{47}$$

A symmetric boundary condition is applied at the center of the specimen ($X_3 = 0$) due to the symmetry of temperature distribution. Using the same initial condition (43), the heat diffusion equation (46) can be solved for $T(X_3,t)$ using the finite difference method. The average temperature variation (44) at the center of the specimen is plotted in Figure 15.

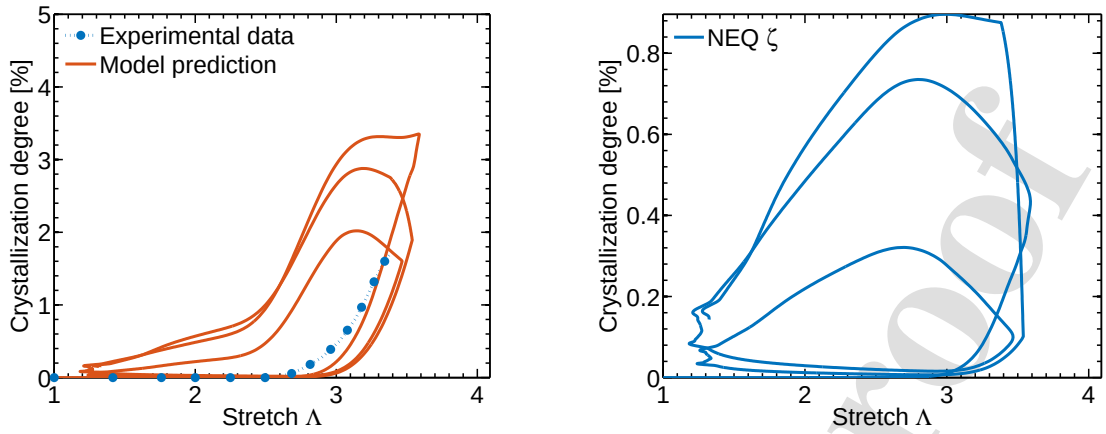

(a) (b)

Figure 14: Evolution of crystallinity in a cyclic biaxial tension with relaxation: a) Total crystallinity, b) Nonequilibrium crystallinity.

One observes good agreement between the numerical result and the experimental data.

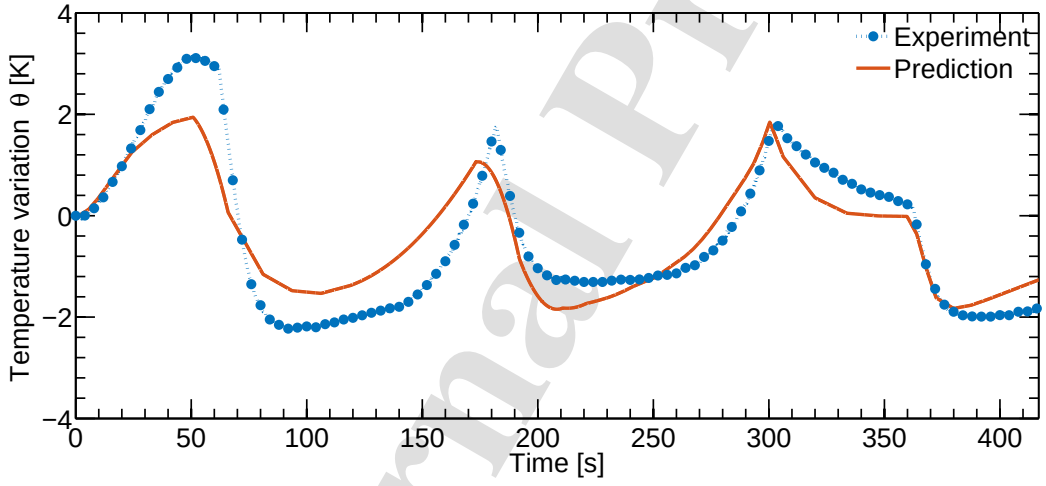

(b)

Figure 15: Time evolution of temperature variation predicted by the proposed model in the biaxial tension.

Remark 4. *Note that the predicted calorimetric responses (temperature variation and heat source) in the current work is independent of the 0D approximation in Part I (Khiêm et al., 2021). While the 0D approach predicts the heat source from the measured temperature variation (i.e. from the left hand side of* (C.9)*), the numerical prediction here based directly*

on the local heat source at a continuum material point (i.e. from the right hand side of (C.9)*). Good agreement with all experimentally measured quantities under different loading cases validates the modeling assumptions utilized here.*

8. Conclusions

In this paper, a theoretical modeling of strain-induced crystallization has been developed. This work thoroughly explains the physical picture of strain-induced crystallization in natural rubbers beyond thermodynamic equilibrium: 1) the stress-strain hysteresis loop is due to both equilibrium and nonequilibrium crystallization. The hysteresis part of equilibrium crystallization results from the internal energy change due to the appearance of a new crystal morphology, whereas the part corresponding to nonequilibrium crystallization is due to the change in the internal energy of crystalline segments, 2) the intrinsic dissipation due to the equilibrium crystallinity is zero, whereas that of the nonequilibrium one is positive, 3) a new type of crystallite (tertiary one) occurs in dynamics loading whose kinetics favors stress relaxation 4) the decrease in stress of natural rubbers during stress relaxation is not only due to viscoelasticity but also the reduction of diffusion velocity of crystalline segments, 5) there is strain-induced crystallization in multiaxial tension, and the crystallinity in this case is larger than that in uniaxial tension at the same macroscopic stretch. Good agreement of the model predictions with abundant experimental evidence under sophisticated loading scenarios (Part I - Khiêm et al. (2021)) validates the physical ground of the proposed model.

The results strongly confirm that the strain-induced crystallization in natural rubbers should be studied from neither solely equilibrium nor solely nonequilibrium thermodynamics. It should be investigated on both.

Appendix A. Analytical network averaging concept

The analytical network averaging concept (Khiêm and Itskov, 2016, 2017, 2018a,b; Khiêm et al., 2019) assumes the existence of an orientational distribution function of polymer strands in rubber-like materials. This distribution function can be derived from a series of

probability density functions ρ_i related to a set of predefined unit vectors $\boldsymbol{E}_i$ $(i = 1, 2, .., m)$ as follows

$$\rho\left(\boldsymbol{n}\right) = \sum_{i=1}^{m} \frac{1}{m} \cdot \tilde{\rho}_i\left(\boldsymbol{n}\right) = \sum_{i=1}^{m} \frac{1}{m} \cdot \rho_i\left(\theta_i, \varsigma_i, \boldsymbol{E}_i\right). \tag{A.1}$$

Therein, m is the number of equidistant collocation points on a half-sphere specifying the deformation-induced anisotropy. Each constituent $\rho_i\left(\theta_i, \varsigma_i, \boldsymbol{E}_i\right)$ of the probability density (A.1) is defined on the basis of the even von Mises-Arnold-Fisher distribution function (Fisher, 1953)

$$\rho_i\left(\theta_i, \varsigma_i, \boldsymbol{E}_i\right) = \frac{\varsigma_i}{4\pi \sinh\left(\varsigma_i\right)} \cosh\left(\varsigma_i \cdot \cos\theta_i\right), \tag{A.2}$$

where θ_i indicates the angle between the directional unit vector $\boldsymbol{n}$ and the vector $\boldsymbol{E}_i$, ς_i denotes the concentration parameter.

According to the analytical network-averaging concept, the mesoscopic stretch at a material point is evaluated as the root mean square of the macroscopic stretch over the unit sphere by taking the directional distribution of polymer strands into account (Khiêm and Itskov, 2016, 2017, 2018a,b; Khiêm et al., 2019)

$$\begin{aligned} \bar{\Lambda} &= \left[\int_S \rho\left(\boldsymbol{n}\right) \overset{\boldsymbol{n}}{\Lambda^2}\, dS\right]^{\frac{1}{2}} = \left[\mathbf{C} : \sum_{i=1}^{m} \frac{1}{m} \int_0^{2\pi} \int_0^{\pi} \rho_i\left(\boldsymbol{n}\right)\, \boldsymbol{n} \otimes \boldsymbol{n}\, \sin\theta_i d\theta_i d\varphi_i\right]^{\frac{1}{2}} \\ &= \left[\sum_{i=1}^{m} \frac{1}{m} \cdot \left(\left(1 - w_i\right) \frac{I_1}{3} + w_i \Lambda_{\mathrm{i}}^2\right)\right]^{\frac{1}{2}}, \end{aligned} \tag{A.3}$$

where $\theta_i \in [0, \pi]$ and $\varphi_i \in [0, 2\pi]$ are spherical coordinates of the vector $\boldsymbol{n}$ with respect to orthonormal vectors based on the collocation directions $\boldsymbol{E}_i$. I_1 denotes the first principal invariant of the right Cauchy-Green tensor $\mathbf{C} = \mathbf{F}^{\mathrm{T}}\mathbf{F}$, and $\Lambda_{\mathrm{i}}^2 = \mathbf{C} : \boldsymbol{E}_i \otimes \boldsymbol{E}_i$ is the square of the macro-stretch in direction $\boldsymbol{E}_i$.

Furthermore, the mesoscopic tube contraction is evaluated as the root mean square of the macroscopic tube contraction. Thus, it can be obtained similar to (A.3) as (Khiêm and

Itskov, 2016, 2017, 2018a,b; Khiêm et al., 2019)

$$\bar{\Upsilon} = \left[\int_S \rho\left(\boldsymbol{n}\right) \overset{\boldsymbol{n}}{\Upsilon}{}^2 \, dS\right]^{\frac{1}{2}} = \left[\sum_{i=1}^{m} \frac{1}{m}\left(\left(1-w_i\right)\frac{I_2}{3} + w_i \Upsilon_i^2\right)\right]^{\frac{1}{2}}, \tag{A.4}$$

where I_2 denotes the second principal invariant of the right Cauchy-Green tensor $\mathbf{C}$, $\Upsilon_i = \sqrt{\text{cof}\mathbf{C} : \boldsymbol{E}_i \otimes \boldsymbol{E}_i}$ is the macro tube contraction in direction i, and $\text{cof}\mathbf{C} = \mathbf{C}^{-\text{T}}\text{det}\mathbf{C}$ is the cofactor of $\mathbf{C}$.

The coefficient w_i is expressed by

$$w_i = \int_0^{2\pi}\int_0^{\pi} \rho_i\left(\theta_i, \varsigma_i, \boldsymbol{E}_i\right)\ \left(\cos^2\theta_i \sin\theta_i - \sin^3\theta_i \cos^2\varphi_i\right) d\theta_i d\varphi_i = \frac{{\varsigma_i}^2 - 3\coth\left(\varsigma_i\right)\varsigma_i + 3}{{\varsigma_i}^2}. \tag{A.5}$$

w_{i} represent fractions of oriented strands (Murthy et al., 1995; Pazur and Prud'homme, 1996) in each direction i $(i = 1, 2, .., m)$ (Khiêm and Itskov, 2018a,b; Khiêm et al., 2019).

Appendix B. Equilibrium crystallization

Equilibrium phase transition in natural rubbers is governed by two steps: formation of a solid cluster of polymer segments (nucleus) in the amorphous network and growth of such cluster (Khiêm and Itskov, 2018b). These steps are referred to as crystallization nucleation and growth, respectively. In this appendix, the evolution of the equilibrium crystallinities during cyclic loading of natural rubbers will be derived from its corresponding directional values.

Appendix B.1. Crystallization nucleation

The primary nucleus is assumed here to be bundle-like with a cylindrical geometry. Each primary nucleus is built by C neighbouring polymer strands. The change in the free energy of a strand due to the formation of a nucleus in a direction i of the microsphere is given by

$$\Delta G = \gamma_t 2Cs + \gamma_s 2\sqrt{\pi Csl} - Csl\Delta\Psi_{\text{i}}, \qquad i = 1, 2, .., m, \tag{B.1}$$

where γ_t is the surface tension at the top surfaces of the crystallite. γ_s is the surface tension at the side of the crystallite. $\Delta\Psi_{\mathrm{i}}$ is the difference in bulk free energies between the semi-crystalline and the amorphous strands. s is the cross-section area of a single polymer chain, and l is the length of the crystallite.

Thus, according to the Lauritzen-Hoffman nucleation theory (Hoffman and Lauritzen, 1961), the critical number of molecules C^* in the nucleus can be obtained by maximizing (B.1) with respect to C

$$C^* = \frac{4\pi\gamma_s^2}{s\Delta\Psi_{\mathrm{i}}^2}. \tag{B.2}$$

Nuclei with the number of molecules larger than this critical value are likely to form solid crystallites. The free energy barrier required for the crystal nucleation is obtained by substituting C^* into (B.1) as

$$\Delta G^* = \frac{8\pi\gamma_t\gamma_s^2}{\Delta\Psi_{\mathrm{i}}^2}. \tag{B.3}$$

By means of statistical mechanics, the equilibrium primary crystallinity in each direction can be given by (Khiêm and Itskov, 2018b)

$$\zeta_{\mathrm{I}i}^{eq} = B_1 \exp\left(-\frac{\Delta G_n^*}{k_{\mathrm{B}}T_0}\right) = B_1 \exp\left(-\frac{8\pi\gamma_t\gamma_s^2}{k_{\mathrm{B}}T\Delta\Psi_{\mathrm{i}}^2}\right), \qquad i = 1, 2, .., m, \tag{B.4}$$

where B_1 is the primary crystallinity constant.

The total secondary crystallinity is a summation of directional crystallinities and is given by

$$\zeta_{\mathrm{I}}^{eq} = \sum_{i=1}^{m} \zeta_{\mathrm{I}i}^{eq}. \tag{B.5}$$

Appendix B.2. Crystallization growth

Under unloading, some crystallites melt and the sample temperature decreases. Due to the reduction of temperature, mobility of molecules reduces and the secondary crystals

grow by aggregation of polymer segments into the critical nuclei (Khiêm and Itskov, 2018b). The probability of the crystallization growth in a direction i is a joint probability of the crystal nucleation P_n and the likelihood P_d that the polymer segments can overcome the aggregation barrier. In other words, the number of secondary crystallites in the direction i, $i = 1, 2, ..., m$, is a multiplication of the number of nuclei n_{n} and the number of grown crystallites n_{g} from each nucleus as

$$n_{\mathrm{ci}} = n_{\mathrm{n}} \cdot n_{\mathrm{g}}. \tag{B.6}$$

In view of (B.4)

$$n_{\mathrm{n}} = n_{\mathrm{U}} \hat{f}\left(\Lambda_{\mathrm{i}}\right), \tag{B.7}$$

where n_{U} is the maximum number of nuclei involved in the crystallization growth and $\hat{f}\left(\Lambda_{\mathrm{i}}\right) = \exp\left(-\dfrac{8\pi\bar{\gamma}_t\bar{\gamma}_s^2}{k_{\mathrm{B}}T_0\Delta\Psi_{\mathrm{i}}^2\left(\Lambda_{\mathrm{i}}\right)}\right)$. Therein, $\bar{\gamma}_t$ and $\bar{\gamma}_s$ are the surface tension at the top and the side of the new type of crystallite, respectively.

The number of grown crystallites n_{g} can be calculated by subtracting the number of melted segments from the number of segments diffused into the crystal nucleus as Khiêm and Itskov (2018b)

$$\begin{aligned} n_{\mathrm{g}} &= n_{\mathrm{G}}\left[\hat{f}\left(\Lambda_{\mathrm{i}}^{\mathrm{c\,max}}\right) - \hat{f}\left(\Lambda_{\mathrm{i}}\right)\right] \\ &= n_{\mathrm{G}}\left[\exp\left(-\frac{8\pi\bar{\gamma}_t\bar{\gamma}_s^2}{k_{\mathrm{B}}T_0\Delta\Psi_{\mathrm{Ui}}^2\left(\bar{\Lambda}_{\mathrm{i}}^{\max}\right)}\right) - \exp\left(-\frac{8\pi\bar{\gamma}_t\bar{\gamma}_s^2}{k_{\mathrm{B}}T_0\Delta\Psi_{\mathrm{Ui}}^2\left(\bar{\Lambda}_{\mathrm{i}}\right)}\right)\right]. \end{aligned} \tag{B.8}$$

The equilibrium secondary crystallinity in each direction is proportional to the number of grown crystallites and therefore reads

$$\zeta_{\mathrm{II}i}^{eq} = B_2\hat{f}\left(\Lambda_{\mathrm{i}}\right)\left[\hat{f}\left(\Lambda_{\mathrm{i}}^{\mathrm{c\,max}}\right) - \hat{f}\left(\Lambda_{\mathrm{i}}\right)\right], \qquad i = 1, 2, .., m, \tag{B.9}$$

where B_2 is the secondary crystallinity constant.

The total secondary crystallinity is a summation of directional crystallinities and is given

by

$$\zeta_{\mathrm{II}}^{eq} = \sum_{i=1}^{m} \zeta_{\mathrm{II}i}^{eq}. \tag{B.10}$$

Appendix C. Thermomechanical framework

The local form of the first law of thermodynamics for a semi-crystalline polymer is given in the Lagrangian description by (Khiêm and Itskov, 2018b)

$$\dot{U} = \mathbf{P} : \dot{\mathbf{F}} - \mathrm{Div}\,\boldsymbol{Q} + \hat{R}, \tag{C.1}$$

where $\boldsymbol{Q}$ is the heat influx per unit reference area, $\hat{R} = \Delta H \dot{\zeta}^{total}$ denotes the internal heat supply per unit reference volume due to phase transition (Khiêm and Itskov, 2018b), $\mathbf{P}$ is the first Piola-Kirchhoff stress tensor and the superposed dot indicates the material time derivative. ΔH is the latent heat of fusion and $\dot{\zeta}^{total}$ is the crystallinity. Assuming Fourier's law, the heat influx per unit current area is given by $\boldsymbol{q} = -k_0 \mathrm{grad} T$. Pulling back to the reference state yields $\boldsymbol{Q} = -k_0 \mathbf{C}^{-1} \mathrm{det}\mathbf{F} \mathrm{Grad} T$.

The second law of thermodynamics can be given in the form of the Clausius-Planck inequality by (Khiêm and Itskov, 2018b)

$$D_{\mathrm{int}} = \mathbf{P} : \dot{\mathbf{F}} - \dot{U} + T\dot{\eta} \geq 0. \tag{C.2}$$

Therein, D_{int} is the mechanical dissipation, which is usually referred to as the intrinsic dissipation in calorimetric studies.

The rate of mechanical dissipation can be further expressed as

$$D_{\mathrm{int}} = \mathbf{P} : \dot{\mathbf{F}} - \frac{\partial U}{\partial T}\dot{T} - \frac{\partial U}{\partial \mathbf{F}} : \dot{\mathbf{F}} - \frac{\partial U}{\partial \boldsymbol{\Xi}} : \dot{\boldsymbol{\Xi}} + T\frac{\partial \eta}{\partial T}\dot{T} + T\frac{\partial \eta}{\partial \mathbf{F}} : \dot{\mathbf{F}} + T\frac{\partial \eta}{\partial \boldsymbol{\Xi}} : \dot{\boldsymbol{\Xi}}, \tag{C.3}$$

where $\boldsymbol{\Xi}$ is the generalized internal variable.

By means of the Coleman-Noll procedure (Coleman and Noll, 1963), the sufficient con-

dition for (C.2) can be given by

$$\mathbf{P} = \frac{\partial U}{\partial \mathbf{F}} - T\frac{\partial \eta}{\partial \mathbf{F}} - p\mathbf{F}^{-\mathrm{T}}, \tag{C.4}$$

$$\frac{\partial U}{\partial T} = T\frac{\partial \eta}{\partial T}, \tag{C.5}$$

$$D_{\mathrm{int}} = -\frac{\partial U}{\partial \boldsymbol{\Xi}} : \dot{\boldsymbol{\Xi}} + T\frac{\partial \eta}{\partial \boldsymbol{\Xi}} : \dot{\boldsymbol{\Xi}} \geq 0, \tag{C.6}$$

where p denotes a Lagrange multiplier arising from the incompressibility constraint. For the sake of simplicity, we neglect the change in volume of natural rubber, and consider it as incompressible.

For the sake of simplicity, we assume that the heat capacity of natural rubbers is a constant, so that its internal energy is given by (Khiêm and Itskov, 2018b)

$$U = c_0 \left(T - T_0\right) + U_{\mathbf{F}} \left(\mathbf{F}, \boldsymbol{\Xi}\right), \tag{C.7}$$

where $c_0 = \rho_0 C$ is the heat capacity per unit reference volume and T_0 is the reference temperature. ρ_0 is the reference mass density and C is the heat capacity (per unit mass) of natural rubber. Thus, in view of (C.5), the entropy of natural rubber read

$$\eta = c_0 \ln\left(\frac{T}{T_0}\right) + N_c s_{\mathbf{F}} \left(\mathbf{F}, \boldsymbol{\Xi}\right), \tag{C.8}$$

where N_c is the number of active chains per unit reference volume and $s_{\mathbf{F}}$ the deformation-dependent entropy of a single chain.

In view of (C.7) the first law can be reformulated as

$$c_0 \dot{T} - \mathrm{Div}\, \boldsymbol{Q} = \left(\mathbf{P} : \dot{\mathbf{F}} - \dot{U}_{\mathbf{F}}\right) + \Delta H \dot{\zeta}^{total}. \tag{C.9}$$

Therein, the local heat source of unfilled natural rubber is defined as

$$\hat{S} = \left(\mathbf{P} : \dot{\mathbf{F}} - \dot{U}_{\mathbf{F}}\right) + \Delta H \dot{\zeta}^{total}. \tag{C.10}$$

Appendix D. Analytical damage-elastoplasticity

According to Khiêm and Itskov (2017), the yield criterion for damage-elastoplasticity in rubber-like materials can be given by

$$\mathbf{y}\left(\mathbf{T},\hat{\mathbf{T}}\right)=\hat{\mathbf{T}}-\mathbf{T}\leq\mathbf{0}\quad\forall\text{ admissible }\hat{\mathbf{T}}, \tag{D.1}$$

where the thermodynamic driving force reads

$$\mathbf{T}=\mathbf{T}\left(\tilde{\boldsymbol{\lambda}}^{\max}\right)=-\frac{\partial\Psi}{\partial\tilde{\boldsymbol{\lambda}}^{\max}}\left(\tilde{\boldsymbol{\lambda}}^{\max},\tilde{\boldsymbol{\lambda}}\right). \tag{D.2}$$

Therein, the internal variable $\tilde{\boldsymbol{\lambda}}^{\max}=\tilde{\lambda}^{\max}\mathbf{I}$ and the observable variable $\tilde{\boldsymbol{\lambda}}=\tilde{\lambda}\mathbf{I}$ are used due to the isotropic damage assumption in the current work (cf. Khiêm and Itskov (2017)).

Since the material should optimize its dissipation due to damage-elastoplastic deformation (Hill, 1948), by maximizing $\mathbf{T}:\dot{\tilde{\boldsymbol{\lambda}}}^{\max}$ subject to the yield condition, the associated flow rule reads (Khiêm and Itskov, 2017)

$$\dot{\tilde{\boldsymbol{\lambda}}}^{\max}=\boldsymbol{\gamma}\frac{\partial\mathrm{y}}{\partial\mathbf{T}}=\boldsymbol{\gamma}, \tag{D.3}$$

$$\tilde{\boldsymbol{\lambda}}^{\max}(0)=\mathbf{I}, \tag{D.4}$$

where γ is the damage-elastoplasticity Lagrange multiplier.

To obtain a rate-independent evolution law, $\gamma\left(\tilde{\boldsymbol{\lambda}},\dot{\tilde{\boldsymbol{\lambda}}}\right)$ should be a linear function with respect to the deformation rate. Thus, in view of (D.3), the damage-elastoplasticity Lagrange multiplier should read

$$\boldsymbol{\gamma}=\dot{\tilde{\boldsymbol{\lambda}}}^{\max}=\frac{d\tilde{\boldsymbol{\lambda}}^{\max}}{d\tilde{\boldsymbol{\lambda}}}\dot{\tilde{\boldsymbol{\lambda}}}. \tag{D.5}$$

The optimality condition is given by (Khiêm and Itskov, 2017)

$$\mathbf{y}:\boldsymbol{\gamma}=0;\quad\boldsymbol{\gamma}\geq\mathbf{0};\quad\mathbf{y}\leq\mathbf{0}. \tag{D.6}$$

According to (D.6), under loading $\boldsymbol{\gamma}\left(\tilde{\boldsymbol{\lambda}}, \dot{\tilde{\boldsymbol{\lambda}}} > \mathbf{0}\right) > \mathbf{0}$, so that in view of (D.5), $\dfrac{d\tilde{\boldsymbol{\lambda}}^{\max}}{d\tilde{\boldsymbol{\lambda}}} > 0$ $\forall \tilde{\boldsymbol{\lambda}}$. Furthermore, under neural loading or unloading $\boldsymbol{\gamma}\left(\tilde{\boldsymbol{\lambda}}, \dot{\tilde{\boldsymbol{\lambda}}} \leq \mathbf{0}\right) = \dot{\tilde{\boldsymbol{\lambda}}}^{\max} = \mathbf{0}$. It can be easily seen that the analytical solution $\tilde{\lambda}^{\max}(t) = \beta^{c-1} \max_{\tau \in [-\infty, t]} \tilde{\lambda}(\tau)$, with the constant $\beta > 1$ and c is a positive natural number, fulfils both conditions. In contrast to Khiêm and Itskov (2017), the solution of internal variable $\tilde{\lambda}^{\max}(t)$ here introduces an isotropic hardening law into the analytical damage-elastoplasticity theory, and β^{c-1} controls the change of the damage surface after a load reversal.

References

Amnuaypornsri, S., Toki, S., Hsiao, B. S., Sakdapipanich, J., 2012. The effects of endlinking network and entanglement to stress-strain relation and strain-induced crystallization of un-vulcanized and vulcanized natural rubber. Polymer 53 (15), 3325–3330.

Arunachala, P. K., Rastak, R., Linder, C., 2021. Energy based fracture initiation criterion for strain-crystallizing rubber-like materials with pre-existing cracks. Journal of the Mechanics and Physics of Solids, 104617.
URL https://www.sciencedirect.com/science/article/pii/S0022509621002593

Aygün, S., Klinge, S., 2020. Continuum mechanical modeling of strain-induced crystallization in polymers. International Journal of Solids and Structures 196-197, 129–139.

Behnke, R., Berger, T., Kaliske, M., 2018. Numerical modeling of time- and temperature-dependent strain-induced crystallization in rubber. International Journal of Solids and Structures 141-142, 15–34.

Brüning, K., Schneider, K., Roth, S. V., Heinrich, G., 2012. Kinetics of strain-induced crystallization in natural rubber studied by WAXD: Dynamic and impact tensile experiments. Macromolecules 45 (19), 7914–7919.

Brüning, K., Schneider, K., Roth, S. V., Heinrich, G., 2015. Kinetics of strain-induced crystallization in natural rubber: A diffusion-controlled rate law. Polymer 72, 52–58.

Candau, N., Laghmach, R., Chazeau, L., Chenal, J.-M., Gauthier, C., Biben, T., Munch, E., 2015. Influence of strain rate and temperature on the onset of strain induced crystallization in natural rubber. European Polymer Journal 64, 244–252.

Coleman, B. D., Noll, W., 1963. The thermodynamics of elastic materials with heat conduction and viscosity. Archive for Rational Mechanics and Analysis 13 (1), 167–178.

Dal, H., Gültekin, O., Açikgöz, K., 2020. An extended eight-chain model for hyperelastic and finite vis-

coelastic response of rubberlike materials: Theory, experiments and numerical aspects. Journal of the Mechanics and Physics of Solids 145.

Dargazany, R., Itskov, M., 2009. A network evolution model for the anisotropic Mullins effect in carbon black filled rubbers. International Journal of Solids and Structures 46, 2967–2977.

Dargazany, R., Khiêm, V. N., Itskov, M., 2014a. A generalized network decomposition model for the quasi-static inelastic behavior of filled elastomers. International Journal of Plasticity 63, 94–109.

Dargazany, R., Khiêm, V. N., Poshtan, E. A., Itskov, M., 2014b. Constitutive modeling of strain-induced crystallization in filled rubbers. Physical Review E 89, 022604.

Fisher, R., 1953. Dispersion on a sphere. Proceedings of the Royal Society of London. Series A, Mathematical and Physical Sciences 217 (1130), 295–305.

Gent, A. N., 1996. A new constitutive relation for rubber. Rubber Chemistry and Technology 69 (1), 59–61.

Gros, A., Huneau, B., Verron, E., Tosaka, M., 2019a. A physically-based model for strain-induce d crystallization in natural rubber . Part I : Life cycle of a crystallite. Journal of the Mechanics and Physics of Solids 125, 164–177.

Gros, A., Tosaka, M., Huneau, B., Verron, E., Poompradub, S., Senoo, K., 2015. Dominating factor of strain-induced crystallization in natural rubber. Polymer 76, 230–236.

Gros, A., Verron, E., Huneau, B., 2019b. A physically-base d model for strain-induce d crystallization in natural rubber . Part II : Derivation of the mechanical model. Journal of the Mechanics and Physics of Solids 125, 255–275.

Guilié, J., Thien-Nga, L., Le Tallec, P., 2015. Micro-sphere model for strain-induced crystallisation and three-dimensional applications. Journal of the Mechanics and Physics of Solids 81, 58–74.

Guo, Q., Zaïri, F., 2020. A physically-based thermo-mechanical model for stretch-induced crystallizable rubbers: Crystallization thermodynamics and chain-network crystallization anisotropy. International Journal of Plasticity 131, 102724.

Guo, Q., Zaïri, F., Guo, X., 2018. Thermodynamics and mechanics of stretch-induced crystallization in rubbers. Physical Review E 97 (5), 1–13.

Hill, R., 1948. A variational principle of maximum plastic work in classical plasticity. The Quarterly Journal of Mechanics and Applied Mathematics 1 (1), 18–28.

Hoffman, J. D., Lauritzen, J., 1961. Crystallization of Bulk Polymers With Chain Folding : Theory of Growth of Lamellar Spherulites. Journal of Research of the National Bureau of Standards-A. Physics and Chemistry 65A (4), 297–336.

Huneau, B., 2011. Strain-induced crystallization of natural rubber: A review of X-ray diffraction investigations. Rubber Chemistry and Technology 84 (3), 425–452.

Katz, J. R., 1925. Rntgenspektrographische Untersuchungen am gedehnten Kautschuk und ihre mgliche

Bedeutung fr das Problem der Dehnungseigenschaften dieser Substanz. Naturwissenschaften 13 (19), 410–416.

Khiêm, V. N., Itskov, M., 2016. Analytical network-averaging of the tube model: Rubber elasticity. Journal of the Mechanics and Physics of Solids 95, 254–269.

Khiêm, V. N., Itskov, M., 2017. An averaging based tube model for deformation induced anisotropic stress softening of filled elastomers. International Journal of Plasticity 90, 96–115.

Khiêm, V. N., Itskov, M., 2018a. Analytical network-averaging of the tube model: Mechanically induced chemiluminescence in elastomers. International Journal of Plasticity 102, 1–15.

Khiêm, V. N., Itskov, M., 2018b. Analytical network-averaging of the tube model: Strain-induced crystallization in natural rubber. Journal of the Mechanics and Physics of Solids 116, 350–369.

Khiêm, V. N., Le Cam, J.-B., Charlès, S., Itskov, M., 2021. Thermodynamics of strain-induced crystallization in filled natural rubber under uni- and biaxial loadings. Part I: Complete energetic characterization and crystallinity evaluation. (submitted).

Khiêm, V. N., Mai, T.-T., Urayama, K., Gong, J. P., Itskov, M., 2019. A Multiaxial Theory of Double Network Hydrogels. Macromolecules 52 (15), 5937–5947.

Kroon, M., 2010. A constitutive model for strain-crystallising rubber-like materials. Mechanics of Materials 42, 873–885.

Laghmach, R., Candau, N., Chazeau, L., Munch, E., 2015. Phase field modelling of strain induced crystal growth in an elastic matrix. The Journal of Chemical Physics 142, 244905.

Loos, K., Aydogdu, A. B., Lion, A., Johlitz, M., Calipel, J., 2020. Strain-induced crystallisation in natural rubber : a thermodynamically consistent model of the material behaviour using a multiphase approach. Continuum Mechanics and Thermodynamics 32 (2), 501–526.

Marckmann, G., Verron, E., Gornet, L., Chagnon, G., Charrier, P., Fort, P., 2002. A theory of network alteration for the Mullins effect. Journal of the Mechanics and Physics of Solids. 50, 2011–2028.

Mistry, S. J., Govindjee, S., 2014. A micro-mechanically based continuum model for strain-induced crystallization in natural rubber. International Journal of Solids and Structures 51 (2), 530–539.

Murakami, S., Senoo, K., Toki, S., Kohjiya, S., 2002. Structural development of natural rubber during uniaxial stretching by in situ wide angle X-ray diffraction using a synchrotron radiation. Polymer 43 (7), 2117–2120.

Murthy, N. S., Bray, R. G., Correale, S. T., Moore, R. A. F., 1995. Drawing and annealing of nylon-6 fibres: studies of crystal growth, orientation of amorphous and crystalline domains and their influence on properties. Polymer 36 (20), 3863–3873.

Nateghi, A., Dal, H., Keip, M.-A., Miehe, C., 2018. An affine microsphere approach to modeling strain-induced crystallization in rubbery polymers. Continuum Mechanics and Thermodynamics 30 (3), 485–

507.

Pazur, R. J., Prud'homme, R. E., 1996. X-ray pole figure and small angle scattering measurements on tubular blown low-density poly(ethylene) films. Macromolecules 29 (1), 119–128.

Plagge, J., Hentschke, R., 2021. Microphase separation in strain-crystallizing rubber. Macromolecules 54 (12), 5629–5635.

Plagge, J., Klüppel, M., 2018. A theory relating crystal size, mechanical response, and degree of crystallization in strained natural rubber. Macromolecules 51 (10), 3711–3721.

Rastak, R., Linder, C., 2018. A non-affine micro-macro approach to strain-crystallizing rubber-like materials. Journal of the Mechanics and Physics of Solids 111, 67–99.

Rault, J., Marchal, J., Judeinstein, P., Albouy, P. A., 2006a. Chain orientation in natural rubber, Part II: 2H-NMR study. The European Physical Journal E 21 (3), 243–261.

Rault, J., Marchal, J., Judeinstein, P., Albouy, P. A., 2006b. Stress-induced crystallization and reinforcement in filled natural rubbers: 2H NMR study. Macromolecules 39, 8356–8368.

Reese, S., Govindjee, S., 1998. A theory of finite viscoelasticity and numerical aspects. International Journal of Solids and Structures 35, 3455–3482.

Saadedine, M., Zari, F., Ouali, N., Tamoud, A., Mesbah, A., 2021. A micromechanics-based model for visco-super-elastic hydrogel-based nanocomposites. International Journal of Plasticity 144, 103042.
URL https://www.sciencedirect.com/science/article/pii/S0749641921001170

Sae-oui, P., Freakley, P. K., Oubridge, P. S., 1999. Determination of heat transfer coefficient of rubber to air. Plastics, Rubber and Composites Processing and Applications 28 (2), 65–68.

Samaca Martinez, J. R., Le Cam, J. B., Balandraud, X., Toussaint, E., Caillard, J., 2013a. Mechanisms of deformation in crystallizable natural rubber. Part 1: Thermal characterization. Polymer 54 (11), 2717–2726.

Samaca Martinez, J. R., Le Cam, J. B., Balandraud, X., Toussaint, E., Caillard, J., 2013b. Mechanisms of deformation in crystallizable natural rubber. Part 2: Quantitative calorimetric analysis. Polymer 54 (11), 2727–2736.

Toki, S., Sics, I., Ran, S., Liu, L., Hsiao, B., 2003. Molecular orientation and structural development in vulcanized polyisoprene rubbers during uniaxial deformation by in situ synchrotron X-ray diffraction. Polymer 44 (19), 6003–6011.

Toki, S., Sics, I., Ran, S., Liu, L., Hsiao, B. S., Murakami, S., Senoo, K., Kohjiya, S., 2002. New insights into structural development in natural rubber during uniaxial deformation by in situ synchrotron X-ray diffraction. Macromolecules 35 (17), 6578–6584.

Tosaka, M., Kawakami, D., Senoo, K., Kohjiya, S., Ikeda, Y., Toki, S., Hsiao, B. S., 2006. Crystallization and stress relaxation in highly stretched samples of natural rubber and its synthetic analogue. Macromolecules

39 (15), 5100–5105.

Wakeshima, H., 1954. Time lag in the self-nucleation. The Journal of Chemical Physics 22 (9), 1614–1615.

V.N.K. and J.-B.L.C.: Conceptualization, Validation **V.N.K.:** Methodology, Software, Formal analysis, Investigation, Visualization, Writing - Original Draft **V.N.K., J.-B.L.C. and M.I.:** Supervision **V.N.K., J.-B.L.C., S.C. and M.I.:** Writing - Review & Editing

Declaration of interests

☒The authors declare that they have no known competing financial interests or personal relationships that could have appeared to influence the work reported in this paper.

☐The authors declare the following financial interests/personal relationships which may be considered as potential competing interests: